Dolomites in hydrated fine-grained Antarctic micrometeorites: Effective tools for analyzing secondary processes

E. Dobrică, K.K. Ohtaki, C. Engrand

Geochimica et Cosmochimica Acta

DOLOMITES IN HYDRATED FINE-GRAINED ANTARCTIC MICROMETEORITES: EFFECTIVE TOOLS FOR ANALYZING SECONDARY PROCESSES

--Manuscript Draft--

Manuscript Number:	
Article Type:	Article
Keywords:	carbonates; micrometeorite; transmission electron microscope; shock metamorphism; asteroid
Corresponding Author:	Elena Dobrica, Ph.D. University of Hawaii at Manoa Honolulu, Hawaii UNITED STATES
First Author:	Elena Dobrica, Ph.D.
Order of Authors:	Elena Dobrica, Ph.D.
	Elena Dobrică
	Kenta K. Ohtaki
	Cecile Engrand
Abstract:	We report detailed transmission electron microscope (TEM) observations of carbonates from one hydrated fine-grained Antarctic micrometeorite (H-FgMM). These carbonates show the occurrence of complex chemical variations and microstructures that provide important evidence regarding the formation and evolution of rarely analyzed H-FgMMs. The chemical variations were identified at both micrometer and nanometer scales, indicating that these carbonates formed under localized fluid conditions that suggest a variable chemical microenvironment. Individual carbonates grew from isolated reservoirs of fluid. Moreover, these carbonates contain manganese amounts almost twice as high as those measured in CM chondrites but similar to those identified in CI chondrites. Their particular compositions indicate reducing and progressively evolving conditions in the fluid from which these carbonates precipitated, probably due to water consumption during phyllosilicates formation. In addition to the compositional variability, microstructural features are pervasive in these carbonates, similar to those described in heavily shocked meteorites indicating that these carbonates were probably modified during shock processes after their formation. Since carbonates are highly susceptible to shock metamorphism, we suggest that it is essential to investigate their structure in detail before interpreting the isotopic measurements related to the time of their formation. Additionally, associated with carbonates, ubiquitous phosphates were identified in the micrometeorite analyzed. Future studies of these mineral associations will provide us further insight into the formation and evolution of asteroids, especially since they were both identified in the surface materials of Ryugu and Bennu.
Suggested Reviewers:	Takaaki Noguchi tngc@mito.ipc.ibaraki.ac.jp
	Falko Langenhorst Falko.Langenhorst@uni-bayreuth.de
	Christine Jilly-Rehak jillyrehak@ssl.berkeley.edu
	Matthew Genge m.genge@imperial.ac.uk
	Matthias van Ginneken Matthias.Van.Ginneken@ulb.ac.be

DOLOMITES IN HYDRATED FINE-GRAINED ANTARCTIC MICROMETEORITES: EFFECTIVE TOOLS FOR ANALYZING SECONDARY PROCESSES

E. Dobrică[1], K. K. Ohtaki[1], and C. Engrand[2]

[1]Hawai‘i Institute of Geophysics and Planetology, School of Ocean, Earth Science, and Technology, the University of Hawai’i at Mānoa, Honolulu, Hawai‘i 96822 USA.

dobrica@hawaii.edu.

[2]Université Paris-Saclay, CNRS/IN2P3, IJCLab, 91405 Orsay Campus, France.

Abstract - We report detailed transmission electron microscope (TEM) observations of carbonates from one hydrated fine-grained Antarctic micrometeorite (H-FgMM). These carbonates show the occurrence of complex chemical variations and microstructures that provide important evidence regarding the formation and evolution of rarely analyzed H-FgMMs. The chemical variations were identified at both micrometer and nanometer scales, indicating that these carbonates formed under localized fluid conditions that suggest a variable chemical microenvironment. Individual carbonates grew from isolated reservoirs of fluid. Moreover, these carbonates contain manganese amounts almost twice as high as those measured in CM chondrites but similar to those identified in CI chondrites. Their particular compositions indicate reducing and progressively evolving conditions in the fluid from which these carbonates precipitated, probably due to water consumption during phyllosilicates formation. In addition to the compositional variability, microstructural features are pervasive in these carbonates, similar to those described in heavily shocked meteorites indicating that these carbonates were probably modified during shock processes after their formation. Since carbonates are highly susceptible to shock metamorphism, we suggest that it is essential to investigate their structure in detail before interpreting the isotopic measurements related to the time of their formation. Additionally, associated with carbonates, ubiquitous phosphates were identified in the micrometeorite analyzed. Future studies of these mineral associations will provide us further insight into the formation and evolution of asteroids, especially since they were both identified in the surface materials of Ryugu and Bennu.

1. Introduction

Carbonates are excellent candidates to study secondary processes that modified the primitive materials that formed in the Solar System (Brearley 2006; Tyra et al. 2013). They have the potential to provide us with a high-fidelity record of environmental conditions and the timing of their formation (Brearley 2006; Tyra et al. 2013; Alexander et al. 2015; Telus et al. 2019). Furthermore, they have been commonly identified in carbonaceous chondrites (<2 vol%), though they are rare in dust particles such as Antarctic micrometeorites (AMMs) and interplanetary dust particles (IDPs, Sandford and Walker 1985; Tomeoka and Buseck 1986; Germani et al. 1990; Rietmeijer 1990; Bradley et al. 1992; Zolensky and Lindstrom 1992; Brearley 2006; Duprat et al. 2007; Aleon et al. 2009; de Leuw et al. 2009; Dobrică et al. 2009; Tyra et al. 2012; Fujiya et al. 2013; Lee et

al. 2014; Alexander et al. 2015; Dobrică et al. 2019). Recently, centimeters-thick, roughly meter-long veins of carbonates were identified in outcrops at the surface of the asteroid Bennu (Kaplan et al. 2020), and curation analyses of asteroid Ryugu also suggest the presence of carbonates in the samples (Yada et al. 2021). Therefore, in preparation for the analyses of returned asteroidal samples, our study expands on earlier efforts to investigate the secondary processes and the alteration conditions of H-FgMMs, with a focus on carbonate crystals (Dobrică et al. 2019). We use site-specific extraction techniques to investigate the mineralogy, texture, chemical compositions of several electron transparent sections extracted from one H-FgMMs described previously using oxygen isotopic measurements (Dobrică et al. 2019). Our detailed TEM observations of carbonates aim to understand a more detailed picture of carbonate formation and evolution of rarely analyzed hydrated micrometeorites.

2. Sample and methods

One unmelted H-FgMMs (03-36-46) was analyzed in this study using extensive TEM techniques. The sample was collected from the pristine Concordia snow during the 2002 campaign (Duprat et al. 2007). The size of the particle analyzed in this study is 84 x 114 µm, which corresponds to the whole particle collected from snow (Fig. 1). The polished and carbon-coated petrographic section was first characterized by scanning electron microscopy (SEM) using backscattered electron imaging on a Helios 660 dual-beam focused ion beam SEM (FIB-SEM) instrument at the Advanced Electron Microscopy Center (AEMC) at the University of Hawai‘i at Mānoa. Four electron transparent sections were prepared by the conventional *in situ* FIB technique (Fig. 1). A platinum protective layer was deposited on top of the region of interest, first by electron beam deposition and then by ion beam deposition, to avoid gallium primary ion beam damage during the FIB sample preparation. The section was transferred to Cu TEM half grids with a micromanipulator. The final ion milling of the 2 µm thick section to electron transparency was carried out with the sample attached to the TEM grid. The final thinning stages were performed at 2 kV with a current of 72 pA. Each FIB section was studied using a variety of TEM techniques, including scanning transmission electron microscopy (STEM) imaging, nanodiffraction, and energy-dispersive X-ray spectroscopy (EDS). All imaging and analysis were carried out at 300 kV using the Titan G2 analytical (S)TEM at AEMC. Crystalline phases were identified by electron nanodiffraction and EDS measurements. Nanodiffraction was carried out with an accelerating

voltage of 300 kV, a camera length of 295 mm, and a convergence angle of 0.1–0.3 mrad. Additional EDS hyperspectral maps were performed at the Molecular Foundry, Lawrence Berkeley National Laboratory using a 80–300 kV TitanX "ChemiSTEM" with four windowless X-ray silicon drift detectors (~0.7 sr solid angle).

The elemental compositions of carbonates reported here were extracted from EDS mapping (at the Molecular Foundry). The EDS maps were collected at 200 kV and displayed using the Esprit 1.9 software package (Bruker Corporation) as color-coded maps. Compositions were normalized to 100%. Oxygen abundances should be viewed with caution because oxygen K X-rays are subject to variable amounts of self-absorption by the sample.

3. Results

3.1 SEM observations

Figure 1 shows the compact fine-grained, unmelted external surface (Fig. 1a) and the polished section (Fig. 1b) of the H-FgMMs (03-36-46) analyzed in this study. In the polished section, several coarse-grained minerals (sulfides, Mg-rich carbonates, Ca-phosphates, and magnetites) were observed embedded in a fine-grained material (Fig. 1b-f). Euhedral to subhedral sulfides (5 x 7 µm, Fig. 1d) and magnetites (3.5 x 7 µm, Fig. 1c) are the largest minerals found at the surface of the polished section. Additionally, multiple anhedral to subhedral, micron-sized Mg-rich carbonates (≤3 x 4.5 µm, Fig. 1c and 1f) and Ca-phosphates (≤2 x 3.5 µm, Fig. 1) are identified by EDS in this micrometeorite. Carbonates represent ~1.4 vol% (~2 μm^2) of the entire surface of the polished section (~150 μm^2) and phosphates cover ~0.6 vol.% (~0.9 μm^2). In this study, we focus on two distinct regions containing carbonates found at ~20 µm distance (Fig. 1b). For simplification purposes, we will call these regions A and B (see Fig. 1b). The carbonates from region A are associated with magnetite (anhedral and framboidal magnetite). The oxygen isotopic compositions of the magnetite-carbonate assemblage (13 x 15 µm in size) were described previously by Dobrică et al. (2019). The largest carbonate crystal in this region is porous and presents multiple fractures (3 x 4.5 µm, Fig. 1c). Additionally, in this region, Ogliore et al. (2019) measured the ^{53}Mn-^{53}Cr systematics in the largest carbonate crystal. Therefore, several crystals in region A could potentially have been modified during the secondary ion mass spectrometry (SIMS, O isotopic measurements, Dobrică et al. 2019) and NanoSIMS measurements (^{53}Mn-^{53}Cr measurements, Ogliore et al. 2019). The carbonate cluster in region B is ~4 x 7 µm in size and has

similar pores and fractures as those observed in the carbonates from region A (Fig. 1f). However, these carbonates remained undamaged since no ion microprobe measurements were performed in this region.

3.2 TEM observations

Four FIB sections were prepared in the H-FgMMs (03-36-46) analyzed in this study. Figure 1c to 1f shows the location of these FIB sections extracted in this study (white rectangles). These regions were selected based on the minerals identified in the polished section by SEM/EDS. Additionally, we selected the regions that were the least damaged by the ion microprobe measurements performed during previous studies (Dobrica et al. 2019, Ogliore et al. 2019). The first FIB sections were extracted from carbonates in region A (UH-001, Fig. 1c) and region B (UH-002, Fig. 1f). The other two FIB sections were extracted from the remaining fine-grained material targeting regions containing micrometer-sized secondary phases such as Ca-phosphates (UH-003, Fig. 1e) and magnetite (UH-006, Fig. 1d).

Carbonates chemistry and microstructures

Detailed TEM observations confirm the presence of multiple carbonate crystals in two different FIB sections (Figs. 2, 4, and 5). They occur both as separate, anhedral, single crystals (Figs. 2a-b and 4, region A) and as a polycrystalline cluster (Figs. 2c-e and 5, region B). The size of the cluster (Fig. 2c-e) in the TEM section is ~1.5 x 3 µm and it has a heterogeneous chemical composition compared to the carbonates identified in region A (Fig. 2a-b). Figure 2d-e shows the Mn and Fe distribution in this large, polycrystalline carbonate cluster (FIB section UH-002). Three distinct regions with variable Mn and Fe concentrations are identified in the EDS maps (2.9-8.1 wt.% MnO, 2.5-6.0 wt.% FeO, Fig. 2c-e). Note that this chemical heterogeneity is not easy to notice in the Z-contrast DF-STEM micrograph (Fig. 2c). These carbonates from region B are in average more enriched in Mn and Fe (Fig. 3, region B - N = 19, 6.1 wt% MnO, S.D. 1.4; 3.1 wt% FeO, S.D. 1.0) compared to those from region A (Fig. 3, region A - N = 8, 4.1 wt% MnO, S.D. 0.7; 2.6 wt% FeO, S.D. 0.4). Figure 3 shows a ternary diagram to compare the $MgCO_3$, $CaCO_3$, and $(Fe+Mn)CO_3$ components (mol%) of carbonates from both regions (region A - dark grey symbols, region B - white and light grey symbols). The chemical compositions measured in the carbonates from 03-36-46 sample indicate the presence of both dolomite and ankerite in this micrometeorite.

The term dolomite is here restricted to material with Mg/Fe ≥ 4:1 (Deer et al. 1992). All carbonates in region A are dolomite crystals (9.9-15.8 Mg/Fe ratio, avg. 10.5, Table 1). According to the diffraction data, the carbonate cluster in region B is composed of two chemically zoned crystals of dolomite, with one of the crystals having an ankeritic rim (Figs. 2 and 5). The Mg/Fe ratio of the largest dolomite crystal in the cluster (left crystal, Fig. 5a) varies from 9.8 Mg/Fe ratio at the top part (LT - left crystal, top part; Fig. 5a) to 9.2 Mg/Fe at the bottom part (LB - left crystal, bottom part; Fig. 5a). The dolomite rim (LB) is Mn-rich (Fig. 2d, 10.21 mol% $MnCO_3$) compared to the top part of the crystal (8.0 mol% $MnCO_3$). Several, Fe-rich inclusions (~20 nm in diameter) were observed in this dolomite rim (LB, Fig. 5b, white arrows); however, the exact mineralogy of these inclusions was not obtained due to the small size of the crystals and that their identification after the regions were damaged during the acquisition of the EDS maps. The smaller crystal in the cluster (right side, Fig. 5) is also chemically zoned, with a dolomite at the top part (RT - right crystal, top part; 9.7 Mg/Fe ratio) and with an ankerite at the bottom part (RB - right crystal, bottom part; 4 Mg/Fe ratio). The bottom part is Mn-poor and Fe-rich (4.7 mol% $MnCO_3$, 8.8 mol% $FeCO_3$) compared to the top part of the crystal (Fig. 5b-c, 8.5 mol% $MnCO_3$, 3.8 mol% $FeCO_3$). Table 1 shows more details about the chemical compositions of the two chemically zoned crystals in the cluster.

All dolomite crystals identified in this study (regions A and B) contain intragranular pores (white arrows, Fig. 4). Additionally, a number of pores are observed at the crystal boundaries, in association with C-rich amorphous material (details described in the next section). The largest intergranular pore identified has ~90 nm in diameter (Fig. 4c). Note the surface of the dolomite crystals (~450 nm in thickness) was damaged during the NanoSIMS measurements (white dashed line, Fig. 4c; Ogliore et al. 2019).

Figures 4 and 5 show the occurrence of complex microstructures of the carbonates identified in this micrometeorite. The most pervasive microstructural features are called modulations and they were observed in carbonates from both A and B regions (Figs. 4b, 5d and 5i). These modulations appear as near-parallel lamellae or domains alternating dark/light contrast when imaged with a small convergence angle (0.1-0.3 mrad) in the STEM mode. The modulations affect the entire crystal and show multiple orientations (Fig. 5d). Additionally, the EDS analysis indicates that these modulations correspond to local compositional variations in manganese up to 2.0 wt% MnO at a few nanometer scale. The black arrows show the location of the Mn-rich regions (Fig. 5, avg. 6.3

wt% MnO compared to the Mn-poor region avg. 7.5 wt% MnO). Figure 5e-f shows the modulation and the Mn distribution in the largest dolomite crystal in the cluster.

Additionally, the interface between the two crystals in the cluster displays a moiré pattern formed by the superimposition of two periodical structures (Figs. 5g-h and 5j). The diffraction pattern obtained on the superposition of the two periodical structures exhibits peaks caused by diffraction on each individual periodical structure (Fig. 5h). Extra peaks due the moiré structure are apparent in the fast Fourier transform (FFT) diffraction pattern made at the boundary between the two crystals (Fig. 5h). Furthermore, the two dolomite crystals show an orientation mismatch of a relative rotation angle of ~4° between lattice fringes of the two carbonates in the cluster (Fig. 5j).

Materials associated with carbonates

All nanometer to micrometer-sized minerals identified in the H-FgAMM analyzed are embedded in a coarse- and fine-grained phyllosilicate matrix (Fig. 6a, coarse-grained phyllosilicates - C-g phyllo.; fine-grained phyllosilicates - F-g phyllo.). The chemical compositions and basal spacing (~0.7-0.9 nm) of the fine-grained phyllosilicates are consistent with serpentine (Fig. 6, Table 1). The coarse-grained phyllosilicates are FeO-rich (26.5 wt% FeO) and SO_3-rich (5.3 wt% SO_3) compared to the fine-grained phyllosilicates (avg. 15 wt% FeO, 1.3 wt% SO_3). Additionally, we identified a subhedral region where phyllosilicates have a compact texture (Fig. 6b, white dashed line). This compact region is composed of phyllosilicates enriched in sulfur (7 wt% SO_3) with an intermediate composition of iron (20.9 wt% FeO) compared to the coarse- and fine-grained phyllosilicates described previously. The chemical compositions of the phyllosilicates are shown in Table 1.

Magnetite is common in this H-FgAMM and was identified in three out of the four FIB sections analyzed in this study. It is present as individual grains embedded in phyllosilicates or as aggregates of framboidal and radial magnetite (Fig. 6c). Framboidal magnetite is the most frequent occurrence, though one with a radial texture was identified in the association with the framboidal magnetite. The size of each framboid magnetite crystal varies from ~0.5 μm to 1.4 μm (Fig. 6). The radial magnetite aggregate (~1.5 x 2.5 μm in size) is composed of fibrous, needle-like, or acicular crystals with sizes up to ~40 nm in width and 1.2 μm in length. Additionally, the individual

crystals of magnetite embedded in fine-grained phyllosilicates range in size from ~0.8 µm to 1.8 µm.

Most sulfides in this micrometeorite are nanometers in size (Fig. 6a, white arrows). However, several micrometers sized (<3.8 x 3.9 µm, Fig. 6d) Ni-poor sulfides (<1.9 at%. S) were identified in all the FIB sections analyzed. Most of these micrometer sulfides contain pores (up to 700 nm in length and 100 nm wide) and have irregular surfaces, with embayments up to ~340 µm long (Fig. 6d).

Two Ca-phosphates [apatite - $Ca_5(PO_4)_3(OH,F,Cl)$] were identified in two different FIB sections (Fig. 6e-f, Table 1). They contain irregular pores with sizes ranging from a few nanometers up to 190 nm (Fig. 6e-f, white arrows).

Additionally, we observed one subhedral, polycrystalline aggregate identified using electron nanodiffraction and EDS measurements as phosphide, more precisely barringerite $(Fe,Ni)_2P$ (Fig. 6b). The aggregate shows embayments (106 nm in length) that are ~3 times smaller than the entire size of the polycrystalline aggregate (~330 x 375 nm).

A C-rich amorphous material was identified in contact with the carbonates from region A (Fig. 2a-b). This carbonaceous matter contains 80.6 wt% C, 15.8 wt% O, and other minor elements, such as 0.9 wt% Mg, 0.3. wt% Si, 0.1 wt% S, 1.3 wt% Ca, 0.9 wt% Mn, and 0.1 wt% Fe. Figure 2b shows the elemental map (C, Mn, and Fe) of the carbonaceous matter (C-rich am.) associated with the carbonates from region A. Most of this carbonaceous matter contains several large pores (up to ~1 µm).

4. Discussion

Carbonates in micrometeorites have been studied previously (Duprat et al. 2007, 2010; Dobrică et al. 2009, 2012). However, although SEM and electron microprobe studies have been performed, they have not received such close examination by TEM as in the present work. The observations presented here focus on the occurrence of complex microstructures and zonations in carbonates (dolomite and ankerite) from one particular micrometeorite (03-36-46) that was previously described by Dobrică et al. (2019) and Ogliore et al. (2019), which report a combined mineralogical, oxygen isotopic measurements, ^{53}Mn-^{53}Cr isotope systematics studies of the magnetite-dolomite assemblage identified in region A (Fig. 1). In the following discussion, we examine the occurrences and the formation processes of the carbonates in different types of

extraterrestrial materials from a perspective gained at the TEM scale. In addition, we examine the implications for the presence of multiple complex microstructural features and their possible role in the interpretation of shock-metamorphic events and the timing of their formation.

4.1. Carbonates occurrence in micrometeorites: A comparison with other extraterrestrial materials

Micrometeorites represent the main source of extraterrestrial matter accreted by the Earth nowadays; however, they are only rarely described as containing carbonates (Love and Brownlee 1993; Duprat et al. 2007; Dobrică et al. 2009; Duprat et al. 2010; Sakamoto et al. 2010; Dobrică et al. 2012; 2019). So far only calcite ($CaCO_3$) and dolomite [$(CaMg)CO_3$] were identified in the AMMs collections and no systematic mineralogical study is currently available. These carbonates are mostly found in fine-grained fluffy and ultracarbonaceous AMMs (Dobrică et al. 2009; Sakamoto et al. 2010). The largest (~14 µm in diameter) euhedral, single-crystal carbonate was identified in an ultracarbonaceous AMM (Duprat et al. 2007; Dobrică et al. 2009; Duprat et al. 2010; Dobrică et al. 2012). Additionally, Noguchi et al. (2002) suggest that phyllosilicate-rich micrometeorites show evidence of the breakdown of carbonate grains when the AMMs entered the Earth's atmosphere.

Similar to AMMs, only rare carbonate crystals were identified so far in interplanetary dust particles (IDPs, Aleon et al. 2009; Tomeoka and Buseck 1986; Zolensky et al. 2008). They occur both as separated euhedral single crystals and as anhedral aggregates with sizes ranging from 50 nm to 2 µm (Aleon et al. 2009; Tomeoka and Buseck 1986; Zolensky et al. 2008). They are typically identified in hydrated IDPs and are associated with Fe-Ni sulfide rather than with magnetite or tochilinite as observed in AMMs and chondritic meteorites (Tomeoka and Buseck 1986; Schramm et al. 1989; Zolensky et al. 2008; Dobrica et al. 2019).

Spectroscopically, carbonates have been detected in outcrops and materials ejected from the surfaces of comets and asteroids, which are likely the main sources of AMMs and IDPs (Lisse et al. 2006, 2007; Wada et al. 2018; Kaplan et al. 2020). The identification of carbonates in the samples returned from the comet 81P/Wild 2 is still debated due to possible contamination issues (Flynn et al. 2008a; Mikouchi et al. 2007; Tomeoka et al. 2008; Wirick et al. 2007). However, imminent analysis of return samples from the asteroids 162173 Ryugu and 101955 Bennu will

improve our understanding of the origin and evolution of carbonates in the small Solar System bodies (Wada et al. 2018; Kaplan et al. 2020).

Tens of different types of carbonates have been identified in meteorites, but calcite, aragonite ($CaCO_3$), dolomite $(Ca,Mg)CO_3$, breunnerite $(Mg,Fe)CO_3$, and siderite ($FeCO_3$) are the principal carbonate phases in chondritic meteorites (CI, CM, CR, CV, CB/CH-like, and OC) (Fredriksson and Kerridge, 1988; Johnson and Prinz, 1993; Weisberg et al. 1993; Riciputi et al., 1994; Endreß and Bishoff, 1996; Benedix et al. 2003; Brearley 2006; Bonal et al. 2010; Rubin and Ma, 2017). Their abundance in chondrites vary up to <4.5 vol%, though they are rare in CV and OC meteorites, and absent in CO chondrites (Zolensky et al. 1997; Brearley 2006; de Leuw et al. 2010; Lee et al. 2012; Tyra 2013; Lee et al. 2014; Alexander et al. 2015; Tyra et al. 2016). Carbonate occurs most commonly as (1) isolated grains and aggregates up to ~150 μm in size distributed in the matrix and chondrule rims of chondrites and (2) veins up to ~25 μm in thickness, crosscutting chondrules and calcium–aluminium-rich inclusions (CAIs, Zolensky et al. 1993; Abreu and Brearley 2005; de Leuw et al. 2010; Verdier-Paoletti et al. 2017; Jilly-Rehak et al. 2018; Vacher et al. 2019). Additionally, Mg-Fe-Ca-bearing carbonates [magnesite - $MgCO_3$, siderite, and ankerite] were identified in all subgroups of Martian meteorites (Gooding 1993; Treiman 1995; Treiman et al. 2000). In Allan Hills (ALH) 84001, an orthopyroxenite and one of the most famous and studied Martian meteorites, carbonates are globular-shaped and compositionally zoned (Mittlefehldt 1994; Treiman 1995; Bridges et al. 2001). They constitute ~1 vol% of the meteorite (Treiman 1995). These carbonates (<30 μm in size) are characterized by two distinct features (1) randomly oriented magnetite crystals (<10 nm to 100 nm) and (2) nm-sized voids (<10 nm to 70 nm) (Bradley et al. 1998; Barber and Scott 2003; Brearley 2003). Most of these features are found to be associated with each other (Brearley 2003). The partially faceted voids identified in carbonates from Allan Hills (ALH) 84001 are generally subrounded similar to those identified the H-FgMMs analysed in this study (see section 4.4).

Though carbonates are scarce components in AMMs compared to meteorite samples, this is probably due to a lack of standardized detection of these phases in these small and difficult to analyze dust particles. Additionally, two additional factors could have played an important factor in the identification of carbonates in micrometeorites, such as (1) terrestrial weathering of AMMs in the ice collections and (2) atmospheric entry heating (Duprat et al. 2007; Noguchi et al. 2012). However, carbonates should be more abundant in H-FgMMs since we show here in this study that

they represent, together with phosphates, the main sink for Ca after being mobilized from glass with embedded metal and sulfides (GEMS), rare chondrules, and CAIs (Dobrică et al. 2009; 2012). It is therefore desirable to achieve in the future a systematic database of the occurrence of carbonates in dust particles (AMMs and IDPs) using non-destructive *in situ* spectroscopic techniques, while avoiding complex sample preparation.

4.2 Carbonate formation processes

Carbonates are generally believed to have formed by parent-body aqueous processing (Brearley 2006; Tyra et al. 2012; Fujiya et al. 2013; Alexander et al. 2015; Doyle et al. 2015). However, it has been suggested that their formation does not necessarily require liquid water and that they could form prior to the accretion of the parent body (Metzler et al. 1992; Kemper et al. 2002; Toppani et al. 2005). Nevertheless, textural evidence (e.g. veins, rims around chondrules, and mineral associations with other secondary, aqueous alteration phases) and complex compositional zoning are supportive of an aqueous alteration scenario (e.g. Brearley 2006). Their formation is consistent with precipitation from aqueous solutions, so their analysis has the potential to provide useful information about the spatial, temporal, and chemical alteration conditions that were present on the parent body of micrometeorites (Brearley and Hutcheon 2002; Brearley 2006; Tyra 2013; Jilly-Rehak et al. 2018; Telus et al. 2019).

Previous studies show that isotopic and chemical variations are ubiquitous in carbonates, regardless of the morphology and sample, indicating changes in fluid composition during their formation (Barber and Scott 2003; Tyra 2013; Tyra et al. 2016). Several studies described the isotopic variations of carbonates (Benedix et al. 2003; Tyra et al. 2016; Telus et al. 2019); however, here we will focus on the compositional variability of carbonates. Generally, compositionally zoned carbonates are commonly observed in chondritic and Martian meteorites with variations at scale ranging from submicron to tens of micrometers (Brearley and Hutcheon, 2000; 2002; Barber and Scott 2006; Bonal et al. 2010; Tyra 2013; Telus et al. 2019). It has been suggested that such variations in composition would require that cation mobility was restricted; otherwise, the compositional zoning pattern in adjacent dolomite grains would be similar. These variations reflect on the local geochemical microenvironments within the parent body of meteorites, in which individual carbonates grew from isolated reservoirs of fluid during aqueous alteration (Brearley et al. 2001; Brearley and Hutcheon 2002; Lee and Ellen 2008; Tyra 2013; Tyra et al. 2016). In CM

chondrites, the compositional zoning in dolomite is heterogeneous with no consistent core-to-rim relationships, suggesting that the crystallization probably started on a substrate with growth occurring into a fluid-filled pore space with very limited communication between pores (Tyra 2013; Tyra et al. 2016). These pores became isolated as a result of serpentinization processes that may have caused a reduction in porosity in the fine-grained materials (Tyra 2013). Therefore, this decreased porosity could have generated localized dissolution reactions that would have controlled the fluid chemistry, resulting in large variations in the dolomite compositions (Tyra 2013; Tyra et al. 2016). Similarly, carbonates in this study exhibit significant localized, compositional variations identified at both (1) micrometer-scale between regions A and B (Fig. 1) and (2) nanometer-scale inside dolomite crystals (Fig. 4). Therefore, according to previous studies, this fine-scale zoning shows that they were formed under localized fluid conditions, which suggests a variable chemical microenvironment, in which individual carbonates grew from isolated reservoirs of fluid.

Furthermore, carbonates in region A deviate from the typical 1:1 Ca-Mg stoichiometry (1.2-1.6 Ca/Mg ratios), displaying excess Ca in the dolomite structure (Fig. 3). We report that the average dolomite in region A has 51.4 mol% $CaCO_3$ and ankerite is 54.8 mol% $CaCO_3$, which shows that their composition is non-stoichiometric. However, the carbonates from region B are stoichiometric overall with $CaCO_3$ values ranging from 49.2 mol% $CaCO_3$ to 50.9 mol% $CaCO_3$ (Fig. 3). Carbonates in CM have been also described as non-stoichiometric, displaying similar excesses in Ca (Fouke and Reeder, 1992; Johnson and Prinz 1993), in addition to the stoichiometric dolomites reported by Zolensky et al. (1997) and Tyra (2013). At the same time, CI chondrites, dolomites display Ca deficiencies compared with the ideal stoichiometry (Johnson and Prinz 1993; Riciputi et al. 1994; de Leuw et al. 2010). All these differences in chemistry between CM and CI dolomites were suggested to result from differences in alteration temperatures of their parent bodies. Nonetheless, Ca excesses was attributed to metastable growth of dolomite at low temperatures or under briny conditions (Fig. 3, Goldsmith and Graf 1960; Fouke and Reeder, 1992; Johnson and Prinz 1993; de Leuw et al. 2010; Tyra 2013). Therefore, here we argue that the chemical zonations observed in the carbonates analyzed in this study indicate changes in fluid composition during low temperature aqueous alteration.

Additionally, we observed that the carbonates in 03-36-46 contain manganese amounts almost twice as high (avg. 10.0 mol% $MnCO_3$, S.D. 2.4, N = 25, range 5.4-13.5 mol% $MnCO_3$) as those measured in CM chondrites (<6.9 mol% $MnCO_3$, de Leuw et al. 2009; Tyra 2016) and Martian

meteorites (<5.2 mole% $MnCO_3$, Mittlefehldt et al. 1994; Treiman 1995), though they are comparable to those in CI chondrites (avg. 6.0 mol% $MnCO_3$, S.D. 4.5, N = 17, range 0.1-19.6 mol% $MnCO_3$; Johnson and Prinz 1993). The highest Mn values are in the carbonates identified in region B (left crystal, rim – LB, 12.1 mol% $MnCO_3$). A substantial source of manganese for these carbonates could be the aqueous alteration of Mg-rich silicates, more precisely, low-iron, manganese-enriched (LIME) pyroxenes and olivines. Notably since LIME minerals were previously identified in AMMs and no Mg-rich silicates were identified in this micrometeorite, suggesting that these phases could have been the main source of Mn to the fluid for the formation of carbonates (Dobrică et al. 2009). Similarly, the high Mg concentrations necessary for the formation of dolomite could have been generated by the replacement of forsterite by serpentine (Sleep et al., 2004; Oze and Sharma, 2007). This is consistent with previous observations indicating that dolomite often forms from brines present once much of the water has been consumed by serpentinization (Tucker and Write, 1990; Arvidson and Mackenzie, 1999).

This manganese enrichment, apart from cation concentration in the fluid, has important information about potential redox reactions of the pore fluids, indicating reducing conditions in the fluids from which the carbonates from 03-36-46 precipitated (Tucker and Wright, 1990; Warren 2000). Furthermore, since Mn tends to increase during later episodes of recrystallisation and considering that carbonates from CM chondrites have Mn-rich zones usually found at grain peripheries, this suggests that the fluids from which these carbonates most likely formed progressively evolved and became more saline with time, perhaps due to the consumption of water during phyllosilicates formation (Brearley and Hutcheon, 2000; Tyra 2013; Tyra et al. 2016). These observations are consistent with mineralogical and geochemical models of progressive aqueous alteration in the CM chondrite parent body (Barnaby and Rimstidt, 1989; Schulte and Shock, 2004; Alexander et al. 2015; Telus et al. 2019).

4.3 Complex microstructures: Evidence of shock deformation

Carbonates in the H-FgMM analyzed (03-36-46) show the presence of fine-scale complex microstructures (modulations, moiré pattern, and pores) that are nevertheless related to several compositional variations (iron-rich inclusions and zonations). These microstructures could be associated either with (1) crystal growth or (2) lattice deformation mechanisms (Gunderson and Wenk 1981; Miser et al 1987; Reeder 1992; Larsson and Christy 2008). Although their evaluation

is not without problems, their interpretation is extremely instructive in elucidating the formation and evolution of carbonate-bearing samples.

Among the variety of microstructures (dislocations, twins, growth zoning, etc.) identified in carbonates from terrestrial samples, modulations got most attention since they were first described about forty years ago (Reeder and Wenk 1979). More precisely dolomite crystals typically exhibit modulations in terrestrial rocks; however, no modulated microstructures were identified in carbonates from extraterrestrial materials (Reksten 1990; Reeder 1992; Rodriguez-Navarro and Ruiz-Agudo 2013). Despite numerous efforts to relate modulations to either compositional variability or strain in the crystal lattice, their origin is still debated (Reksten 1990; Baronnet 1992; Reeder 1992; Martinez et al. 1995; Rodriguez-Navarro and Ruiz-Agudo 2013). In this study, manganese variations recall the modulation microstructures; however, these variations do not perfectly overlay with the shape and orientation of modulations (Fig. 5d-f). This imperfection may be due to the fact that the EDS maps and STEM micrographs were not taken at the same crystallographic orientation. Therefore, looking solely at the nanometric variations of these carbonates, it is unclear if these modulations are evidence of growth processes during a periodic variation in fluid composition, lattice strain, or both.

An alternative way to understand the evolution of the parent body of this H-FgMM is to examine the other microstructures and features identified in these carbonates (e.g., moiré patterns and pores). In particular, the moiré patterns, which have been extensively used in the past for measurement and analysis of strain (Theocharis 1969; Wang 1992; Sirohi and Chau 1999; Wang et al. 2015). These features are generally described to appear whenever two periodical structures are superimposed or stacked with a twist angle and/or lattice mismatch (Latychevskaia et al. 2019; Reidy et al. 2021). They were previously identified in chondritic (CM, CV, CV) and Martian meteorites, as well as in dust particles from comet 81P/Wild 2 captured by the NASA Stardust spacecraft (Tomeoka and Buseck 1990; Barber and Scott 2006; Buseck and Hua 1993; Abreu et al. 2017; De Gregorio et al. 2017). Different mineral phases, including carbonates, olivine, phyllosilicates, and presolar hibonite and carbide grains were described as containing moiré patterns (Tomeoka and Buseck 1990; Leitner et al. 2012; Abreu et al. 2017). Their presence was constantly described as reminiscent of deformation (Tomeoka and Buseck 1990; Leitner et al. 2012; Abreu et al. 2017). Additionally, the occurrence of carbonates with moiré patterns showing a local lattice mismatch were previously described in the heavily shocked Martian meteorite, Allan

Hills 84001 (shock pressures of ~35–40 GPa; Barber and Scott 2006). Although Barber and Scott (2006) did not directly connect these patterns to shock, Brearley (2003) described the carbonates from ALH 84001 as extensively strained as a result of multiple shock events. Therefore, we argue that the occurrence of moiré patterns at the interface between the two dolomite crystals in the carbonate cluster indicates that deformation processes produced during shock metamorphism were active on the parent body of the micrometeorite analyzed. No other evidence of deformation, indicating that the sample experienced shock-induced metamorphic effects, were identified. However, the lack of minerals regularly used in the shock classification scheme of meteorites (olivine, pyroxenes, and feldspars) precludes the evaluation of the degree of shock in this micrometeorite (Stoffler et al. 1991; Scott et al. 1992; Rubin et al. 1997).

Additionally, the presence of pores associated with carbonates have important implications in the investigation of shock metamorphism as well. For example, in the Fe-bearing carbonate from ALH 84001, numerous pores are frequently associated with magnetite inclusions and were interpreted as shock heating features (Brearley 2003). More precisely, their presence was interpreted as the consequence of the loss of CO_2 resulting from the decomposition of the siderite component in solid solution in the carbonate, via decarbonation reactions produced as a consequence of the shock heating of ALH 84001 (Brearley 2003). Similar features are commonly observed in the carbonates identified in this study and the adjacent phases (phosphates and C-rich amorphous material, Figs. 2, 4, and 6). However, they are not associated with magnetite as observed in ALH 84001 (Brearley 2003), though several nanometric Fe-rich inclusions were identified in the dolomite grains (Fig. 5). The absence of clear evidence of magnetite inclusions in the carbonates from the H-FgMM analyzed could be explained by a (1) reduced degree of shock-induced metamorphism experienced by this micrometeorite and/or (2) lower Fe-rich carbonate compositions than those described in ALH 84001 (Fig. 3).

Multiple studies of shock response of carbonate targets in nature, experiments, and numerical models are reported in the literature (Osinski et al. 2008; Langenhorst and Deutsch 2012; Bell 2016; Hamann et al. 2018). However, despite the multitude of different approaches, the reaction of carbonate-bearing targets to hypervelocity impact is not well understood and sometimes yields contrasting results. Furthermore, detailed TEM studies of the shocked materials are scarce. A recent TEM study shows that shocked calcite crystals to pressures varying from 9 GPa to ~61 GPa display a systematic increase in the density of strain features (mottled contrast and twins) with

increasing shock pressure (Bell 2016). In calcite crystals recovered from shock experiments produced at nominal pressure of 85 GPa, vesicles were reported by Langenhorst et al. (2000a, 2000b) and Langenhorst and Deutsch (2012). Therefore, we conclude that the carbonates in this study display multiple evidence of shock. These are the first evidence of shock in carbonates from micrometeorites, although impact-induced shock deformation features such as orientation of dehydration cracks and fracture networks were first described in fine-grained micrometeorites by Suttle et al. (2017).

4.4 Implications of shock modified carbonates

Carbonates have been extensively used to constrain the time scales of aqueous alteration of meteorite parent bodies (Hutcheon et al. 1999; Petitat et al. 2011; Tyra et al. 2012; Lee et al. 2013). However, they are highly susceptible to shock metamorphism because the bonding between Ca cations and CO_3 groups is rather weak, allowing this structure to cleave and to deform easily (Nicolas and Poirier 1976; Langenhorst 2002). Therefore, shock events could potentially disturb the isotope chronometers measured in these phases. As a consequence, it is important to characterize and understand the shock effect before interpreting the isotopic measurements related to age dating as discussed by Fritz et al. (2017). Notably, this is important to be taken into account since several studies suggest that young carbonate age measured in CM, CR, and CH/CB chondrites could have resulted from discrete impact-related events on their parent bodies (Tyra et al. 2012; Lee et al. 2013; Van Kooten et al. 2016; Jillly-Rehak et al. 2017).

Our TEM study shows evidence that carbonates in micrometeorites could have been modified during shock processes after their formation. Therefore, we suggest that it is essential to investigate in detail the structure of carbonates at the TEM scale before interpreting the isotopic measurements related to time of their formation (Fritz et al. 2017). However, further studies are needed to be carried out to fully assess if the wide range of alteration ages observed in chondrites is generated by shock-driven isotopic disturbance (Jillly-Rehak et al. 2017).

Additionally, our study indicates that carbonates could possibly be important candidates in the shock-metamorphism classification scheme, especially in hydrated clasts that lack minerals regularly used in the shock classification scheme of meteorites (olivine, pyroxenes, and feldspars, Stoffler et al. 1991; Scott et al. 1992; Rubin et al. 1997).

4.5 Other minerals associated with carbonates: Clues to parent body evolution

In this study, the carbonates are associated with a variety of (1) secondary phases (phosphates, magnetite, and phyllosilicates) and (2) features (embayments, pores, and pseudomorphic replacements of primary phases) indicating extensive aqueous alteration processes (Fig. 6; e.g. Brearley 2006). No clear evidence of primary phases that have entirely escaped the alteration event(s) were identified. Even the phosphide, barringerite, which is a high-temperature phase, formed at very low fugacity values rather than the product of aqueous alteration contains embayments indicating dissolution processes in the presence of aqueous fluids. Therefore, a remarkable amount of lines of evidence indicates that water was widely available on the parent body of this micrometeorite. Previous studies discuss the existence of these widespread aqueous alteration processes in chondrites and micrometeorites (Kerridge et al. 1979; Schramm et al. 1989; Rowe et al. 1994; Genge et al. 1997, 2008; Noguchi et al. 2002, 2017; Brearley 2006; Zolensky et al. 2008; Blinova et al. 2014; Doyle et al. 2015; Jilly-Rehak et al. 2018; Dobrică and Brearley 2021). Thus, in this section, we focus on the phosphorus-rich phases, since (1) they can provide us further clues relevant to the secondary processes that affected this micrometeorite and (2) they have never been characterized in micrometeorites at such a fine scale.

Two different phosphorus-rich phases (phosphates - apatite and phosphides - barringerite) were identified in the H-FgMM analyzed. However, apatite is the dominant phosphorus reservoir. Recently, phosphates have been documented at the surface materials of the asteroid Ryugu by the MicroOmega investigation onboard Hayabusa2 (Bibring et al. 2017). Phosphates have been identified as a minor phase in many chondrites (CM, CV, CO, OC, etc.), though their presence in ordinary chondrites (OCs) have received most of the attention (Ruzicka et al. 2005; Brearley and Chizmadia 2005; Jilly and Huss 2012; Martin et al. 2013; Jones et al. 2014, 2016; Lewis and Jones 2016; Ward et al. 2017). Previous studies have shown that phosphates in OCs are secondary minerals that form in response to thermal metamorphism (Jones et al. 2014, 2016; Lewis and Jones 2016). Their abundance in all three ordinary chondrite groups shows a small increase with the increase of the petrologic type, particularly between type 4 (0.4 vol.%) and types 5, 6 (0.5 vol.%), when averaged across phosphate abundances of individual H, L, and LL chondrites. The H-FgMM analyzed in this study contains an important amount of phosphates (0.6 vol.%), which is similar to the abundance in equilibrated ordinary chondrites (EOCs) (Lewis and Jones 2016). However, this sample is chemically and texturally unequilibrated and experienced only a low intensity of thermal

metamorphism. According to Dobrică et al. (2019), the estimated temperatures (160-280°C) inferred from the precipitation of magnetite and dolomite are similar to those of thermal metamorphism in unequilibrated OCs. Therefore, the amount of phosphate in this micrometeorite is higher compared to the values measured in EOCs, especially, knowing that this sample is not metamorphosed; however, the amount of phosphate is within the limits of phosphates in carbonaceous chondrites (<1 vol.%, Martin et al. 2013; Ward et al. 2017).

All phosphates identified in this micrometeorite contain a high amount of intragranular pores (Fig. 6). These intragranular pores were previously observed in both phosphates from LL chondrites and terrestrial analogs (Engvik et al., 2009; Jones et al. 2014). Though, secondary porosity can form on the parent body during or after accretion and can be physical or chemical in nature; the development of porosity in phosphates from chondrites was interpreted to result typically during dissolution-reprecipitation mechanisms throughout multiple episodes of aqueous alteration (Jones et al. 2014). Therefore, we suggest that the pores in the apatite crystals formed during aqueous alteration processes, although their formation during shock metamorphism cannot be excluded. Previous studies suggest that phosphates are among the first phases affected by decomposition and vaporization, because they preferentially lose their volatile species, when affected by shock-induced temperature increase (Krzesińska and Almeida 2019). However, experimentally shocked phosphates do not indicate the formation of pores in phosphates (Adcock et al. 2017; Krzesińska and Almeida 2019), though no detailed TEM studies were performed on these shocked samples.

Barringerite, the other phosphorus-rich phase identified in 03-36-46, could provide a significant constraint on the history of this sample. According to previous studies, barringerite is the low-pressure phase of phosphide and allabogdanite is the high-pressure polymorph in the Fe–Ni–P system (Britvin et al. 2019). The presence of barringerite-bearing phosphide in this micrometeorite could indicate that this sample experienced maximum peak pressures of <8 GPa and temperatures of <800°C (Britvin et al. 2019). However, recently, Litasov et al. (2020) have challenged this view showing that both experimental and theoretical studies indicate that allabogdanite is not necessarily associated with high pressure materials. Therefore, further research is needed to understand if these phosphorus-rich accessory minerals can provide us with additional clues related to the temperature and pressure limits experienced by the parent body of micrometeorites.

5. Conclusions

We report the first detailed TEM study of carbonates identified in the Antarctic micrometeorite collections. The observations focus on the occurrence of complex chemical zonations and microstructural features that provide us evidence of the carbonate formation and evolution of the parent body of micrometeorites. Based on our electron microscopy study, we show that the composition of fluids responsible for the alteration of this micrometeorite have varied locally during the carbonate's growth, probably from isolated reservoirs of fluid enriched in manganese. This enrichment, apart from cation concentration in the fluid, has important information about the potential redox reactions of the pore fluids, indicating reducing conditions in the fluids that were present on the parent body of this micrometeorite. Furthermore, we suggest that these carbonates form from brines present once much of the water has been consumed by serpentinization. A substantial source of manganese for these carbonates could be the aqueous alteration of Mg-rich silicates, notably LIME minerals previously identified in AMMs.

Additionally, we show that carbonates in this micrometeorite record multiple evidence of shock. These results are fundamental because they have implication in the interpretation of the isotopic measurements related to time of their formation. Additionally, we suggest that carbonates should be considered as important candidates in the shock-metamorphism classification scheme, especially in samples that lack minerals regularly used in the shock classification scheme of meteorites. Further studies of carbonates from meteorites that exhibit different shock metamorphosis stages would allow us to constrain the temperature and pressure limits experienced by the parent body of micrometeorites. Additionally, their association of phosphates, yet identified at the surface of the asteroid Ryugu could provide us a record of interactions with parent body fluids. Therefore, they may be useful recorders of the metamorphic environment and hence help to interpret metamorphic conditions on asteroids.

Acknowledgments: The Antarctic Micrometeorite collection at Dome C benefits from the logistical help from IPEV and PNRA. This work was supported by ANR (Project COMETOR 18-CE31-0011), Region Ile de France (DIM-ACAV), PNP, CNES, IN2P3 and Labex P2IO in France. We would also like to thank Dr. John Bradley for many helpful comments and discussions. Electron microscopy was performed in the Advanced Electron Microscopy Center (AEMC) at the University of Hawai‘i at Mānoa and the Molecular Foundry. Work at the Molecular Foundry was

supported by the Office of Science, Basic Energy Sciences and U.S. Department of Energy. This work was funded by NASA grant NNH16ZDA001N to E. Dobrica (PI).

References:

Abreu N. M. and Brearley A. J. (2005) Carbonates in Vigarano: Terrestrial, preterrestrial, or both? *Meteorit. Planet. Sci.* **40**, 609–625.

Abreu N. M. and Crispin K. L. (2017) Thermal metamorphism in the CM parent body - Evidence from weakly altered CM chondrites Lapaz Icefield 04565 and 02333. (abstract #6365) *80th Annual Meeting of the Meteoritical Society*.

Adcock C. T., Tschauner O., Hausrath E. M., Udry A., Luo S. N., Cai Y., Ren M., Lanzirotti A., Newville M., Kunz M. and Lin C. (2017) Shock-transformation of whitlockite to merrillite and the implications for meteoritic phosphate. *Nat. Communications* **8**, 14667.

Arvidson R. S. and Mackenzie F. T. (1999) The dolomite problem: Control of precipitation kinetics by temperature and saturation state. *American Journal of Science* **299**, 257-288.

Aléon J., Engrand C., Leshin L. A. and McKeegan K. D. (2009) Oxygen isotopic composition of chondritic interplanetary dust particles: A genetic link between carbonaceous chondrites and comets. *Geochim. Cosmochim. Acta* **73**, 4558–4575.

Alexander C. M. O'D., Bowden R., Fogel M. L. and Howard K. T. (2015) Carbonate abundances and isotopic compositions in chondrites. *Meteorit. Planet. Sci.* **50**, 810–833.

Barber D. J. and Scott E. R. D. (2003) Transmission electron microscopy of minerals in the Martian meteorite Allan Hills 84001. *Meteorit. Planet. Sci.* **38**, 831-848.

Barber D. J. and Scott E. R. D. (2006) Shock and thermal history of Martian meteorite Allan Hills 84001 from transmission electron microscopy. *Meteoritics* **41**, 643-662.

Barnaby R. J. and Rimstidt J. D. (1989) Redox conditions of calcite cementation interpreted from Mn and Fe contents of authigenic calcites. *Geol. Soc. Am. Bull.* **101**, 795–804.

Baronnet A., Cuif J. P., Dauphin Y., Farrc B. and Nouet J. (2008) Crystallization of biogenic Ca-carbonate within organo-mineral micro-domains. Structure of the calcite prisms of the Pelecypod Pinctada margaritifera (Mollusca) at the submicron to nanometre ranges. *Mineralogical Magazine* **72**, 617-626.

Beck P., Gillet Ph., El Goresey A. and Mostefaoui S. (2005) Timescales of shock processes in chondritic and Martian meteorites. *Nature* **435**, 1071–1074.

Bell M. S. (2016) CO_2 release due to impact devolatilization of carbonate: Results of shock experiments. *Meteorit. Planet. Sci.* **51**, 619–646.

622 Benedix G. K., Leshin L. A., Farquhar J., Jackson T. and Thiemens M. H. (2003) Carbonates in
623 CM2 chondrites: Constraints on alteration conditions from oxygen isotopic compositions and
624 petrographic observations. *Geochim. Cosmochim. Acta* **67**, 1577–1588.
625 Blinova A. (2013) Understanding the alteration of the Tagish Lake meteorite through mineralogy,
626 geochemistry and oxygen isotopes. Ph. D. thesis, Univ. of Alberta.
627 Blinova A. I., Zega T. J., Herd C. D. K. and Stroud R. M. (2014) Testing variations within the
628 Tagish Lake meteorite I: Mineralogy and petrology of pristine samples. *Meteorit. Planet. Sci.*
629 **49**, 473–502.
630 Bonal L., Huss G. R., Krot A. N. and Nagashima K. (2010) Chondritic lithic clasts in the CB/CH-
631 like meteorite Isheyevo: Fragments of previously unsampled parent bodies. *Geochim.*
632 *Cosmochim. Acta* **74**, 2500–2522.
633 Brearley A. J. and Chizmadia L. J. (2005) On the behavior of phosphorus during the aqueous
634 alteration of CM2 carbonaceous chondrites. (abstract #2176) 36th Annual Lunar and Planetary
635 Science Conference.
636 Bradley J. P., Humecki H. J. and Germani M. S. (1992) Combined infrared and analytical electron
637 microscope studies of interplanetary dust particles. *The Astronomical Journal* 394, 643.
638 Bradley J. P., McSween H. Y., Jr. and Harvey R. P. (1998) Epitaxial growth of nanophase
639 magnetite in martian meteorite Allan Hills 84001: Implications for biogenic mineralization.
640 *Meteorit. Planet. Sci.* **33**, 765–773.
641 Brearley A. J. (2006) The action of water. In *Meteorites and the early solar system II* (eds. D. S.
642 Lauretta and H. Y. McSween). University of Arizona Press, Tucson, pp. 584–624.
643 Brearley A. J., Hutcheon I. D. and Browning L. (2001) Compositional zoning and Mn-Cr
644 systematics in carbonates from the Y791198 CM2 carbonaceous chondrite (abstract #1458),
645 *32nd Lunar and Planetary Science Conference*.
646 Brearley A. J. and Hutcheon I. D. (2000) Carbonates in the CM1 chondrite ALH84034: mineral
647 chemistry, zoning and Mn–Cr systematics. Lunar Planet. Sci. (abstract #1407), *31nd Lunar and*
648 *Planetary Science Conference*.
649 Brearley A. J. and Hutcheon I. D. (2002) Carbonates in the Y-791198 CM2 chondrite: Zoning and
650 Mn-Cr systematic (abstract). *Meteorit. Planet. Sci.* **37**, A23.
651 Brearley A. J. (2003) Magnetite in ALH 84001: An origin by shock-induced decomposition of
652 iron carbonate. *Meteorit. Planet. Sci.* **38**, 849-870.

Bridges J. C., Catling D. C., Saxton J. M., Swindle T. D., Lyon I. C. and Grady, M. M. (2001) Alteration assemblages in Martian meteorites: Implications for near-surface processes. *Space Science Reviews*, **96**, 365-392.

Britvin S. N., Shilovskikh V. V., Pagano R., Vlasenko N. S., Zaitsev A. N., Krzhizhanovskaya M. G., Lozhkin M. S., Zolotarev A. A. and Gurzhiy V. V. (2019) Allabogdanite, the high-pressure polymorph of $(Fe,Ni)_2P$, a stishovite-grade indicator of impact processes in the Fe–Ni–P system. *Scientific Reports* **9**, 1047.

Buseck P. R. and Hua X. (1993) Matrices of carbonaceous chondrite meteorites. *Annual Review Of Earth And Planetary Sciences* **21**, 255-305.

Deer W. A., Howie R. A. and Zussman J. (1992) An introduction to the rock-forming minerals. 2nd edition. London (Longman Scientific & Technical), 696 pp.

De Gregorio B. T., Stroud R. M., Nittler L. R. and Kilcoyne A. L. D. (2017) Evidence for reduced, carbon-rich regions in the solar nebula from an unusual cometary dust particle. *The Astrophysical Journal* **848**, 113 (11pp).

de Leuw S. Rubin A. E., Schmitt A. K. and Wasson J. T. (2009) ^{53}Mn–^{53}Cr systematics of carbonates in CM chondrites: Implications for the timing and duration of aqueous alteration. *Geochim. Cosmochim. Acta* **73**, 7433-7442.

de Leuw S., Rubin A. E. and Wasson J. T. (2010) Carbonates in CM chondrites: complex formational histories and comparison to carbonates in CI chondrites. *Meteorit. Planet. Sci.* **45**, 513–530.

Dobrică E., Engrand C., Duprat J., Gounelle M., Leroux H., Quirico E. and Rouzaud J. (2009) Connection between micrometeorites and Wild 2 particles: From Antarctic snow to cometary ices. *Meteorit. Planet. Sci.* **1661**, 1643–1661.

Dobrică E., Engrand C., Leroux H., Rouzaud J. N. and Duprat J. (2012) Transmission electron microscopy of CONCORDIA ultracarbonaceous Antarctic micrometeorites (UCAMMs): Mineralogical properties. *Geochim. Cosmochim. Acta* **76**, 68–82.

Dobrică E., Ogliore R. C., Engrand C., Nagashima K. and Brearley A. J. (2019) Mineralogy and oxygen isotope systematics of magnetite grains and a magnetite-dolomite assemblage in hydrated fine-grained Antarctic micrometeorites. *Meteorit. Planet. Sci.* **54**, 1973-1989.

Dobrica E. and Brearley A. J. (2021) Iron-rich olivine in the unequilibrated ordinary chondrite, MET 00526: Earliest stages of formation. *Meteorit. Planet. Sci.* **55**, 2652-2669.

Doyle P. M., Jogo K., Nagashima K., Krot A. N., Wakita S., Ciesla F. J. and Hutcheon I. D. (2015) Early aqueous activity on the ordinary and carbonaceous chondrite parent bodies recorded by fayalite. *Nature Communications* **6**, 7444.

Duprat J., Engrand C., Maurette M., Kurat G., Gounelle M. and Hammer C. (2007) Micrometeorites from Central Antarctic snow: The CONCORDIA collection. *Advances in Space Research* **39**, 605-611.

Duprat J., Dobrică E., Engrand C., Aléon J., Marrocchi Y., Mostefaoui S., Meibom A., Leroux H., Rouzaud J.-N., Gounelle M. and Robert F. (2010) Extreme deuterium excesses in ultracarbonaceous micrometeorites from central Antarctic snow. *Science* **328**, 742–745.

Endreß M. and Bishoff A. (1996) Carbonates in CI chondrites: clues to parent body evolution. *Geochim. Cosmochim. Acta* **60**, 489–507.

Engvik A. K., Golla-Schindler U., Berndt J., Austrheim H. and Putnis A. (2009) Intragranular replacement of chlorapatite by hydroxy-fluor-apatite during metasomatism. *Lithos* **112**, 236-246.

Fouke B. W. and Reeder R. J. (1992) Surface structural controls on dolomite composition - Evidence from sectoral zoning. *Geochim. Cosmochim. Acta* **56**, 4015-4024.

Fredriksson K. and Kerridge J. F. (1988) Carbonates and sulfates in CI chondrites: formation by aqueous activity on the parent body. *Meteoritics* **23**, 35–44.

Fritz J., Greshake A. and Fernandes V. A. (2017) Revising the shock classification of meteorites. *Meteorit. Planet. Sci.* **52**, 1216-1232.

Fujiya W., Sugiura N., Sano Y. and Hiyagon H. (2013) Mn-Cr ages of dolomites in CI chondrites and the Tagish Lake ungrouped carbonaceous chondrite. *Earth Planet. Sci. Lett.* **362**, 130–142.

Genge M. J., Grady M. M. and Hutchison R. (1997) The textures and compositions of fine-grained Antarctic micrometeorites: Implications for comparisons with meteorites. *Geochim. Cosmochim. Acta* **61**, 5149–5162.

Genge M. J., Engrand C., Gounelle M. and Taylor S. 2008. The classification of micrometeorites. *Meteorit. Planet. Sci.* **43**, 497–515.

Germani M. S., Bradley J. P. and Brownlee D. E. (1990) Automated thin film analyses of hydrated interplanetary dust particles in the analytical microscope. *Earth Planet. Sci. Lett.* **101**, 162–179.

Goldsmith J. R. and Graf D. L. (1960) Subsolidus relations in the system $CaCO_3$-$MgCO_3$-$MnCO_3$. *The Journal of Geology*, **68**, 324-335.

715 Gooding J. L. (1993) Aqueous geochemistry on Mars: Possible clues from salts and clays in SNC
716 meteorites. *Workshop on Chemical Weathering on Mars. Lunar and Planetary Institute*
717 *Workshop*, p. 16.
718 Gross G. A. (1965) Geology of iron deposits in Canada, Department of Mines and Technical
719 Surveys, Geological Survey of Canada, Ottawa.
720 Gunderson S. H. and Wenk H. R. (1981) Heterogeneous microstructures in oolitic carbonates.
721 *American Mineralogist* **66**, 789-800.
722 Hamann C., Bläsing S., Hecht L., Schäffer S., Deutsch A., Osterholz J. and Lexow B. (2018) The
723 reaction of carbonates in contact with laser-generated, superheated silicate melts: Constraining
724 impact metamorphism of carbonate-bearing target rocks. *Meteorit. Planet. Sci.* **53**, 1644-1686.
725 Hutcheon I. D., Weisberg M. K., Phinney D. L., Zolensky M. E., Prinz M., and Ivanov A. V.
726 (1999) Radiogenic ^{53}Cr in Kaidun carbonates: Evidence for very early aqueous alteration
727 (abstract #1722). *30th Lunar and Planetary Science Conference*.
728 Jilly C. E. and Huss G. R. (2012) Heterogeneous aqueous alteration in the CR2 chondrite Renazzo.
729 (abstract #1348) Lunar Planet. Sci. Con. XLIII.
730 Jilly-Rehak C. E., Huss G. R. and Nagashima K. (2017) ^{53}Mn-^{53}Cr radiometric dating of secondary
731 carbonates in CR chondrites: Timescales for parent body aqueous alteration. *Geochim.*
732 *Cosmochim. Acta* **201**, 224–244.
733 Jilly-Rehak C. E., Huss G. R., Nagashima K., Schrader D. L. (2018) Low-temperature aqueous
734 alteration on the CR chondrite parent body: Implications from in situ oxygen-isotope analyses.
735 *Geochim. Cosmochim. Acta* **222**, 230-252.
736 Johnson C. A. and Prinz M. (1993) Carbonate compositions in CM and CI chondrites, and
737 implications for aqueous alteration. *Geochim. Cosmochim. Acta* **57**, 2843–2852.
738 Johnson J. E., Webb S. M., Ma C. and Fisher W. W. (2016) Manganese mineralogy and diagenesis
739 in the sedimentary rock record. *Geochim. Cosmochim. Acta* **173**, 210-231.
740 Jones R. H., McCubbin F. M., Dreeland L., Guan Y., Burger P. V. and Shearer C.K. (2014)
741 Phosphate minerals in LL chondrites: A record of the action of fluids during metamorphism on
742 ordinary chondrite parent bodies. *Geochim. Cosmochim. Acta* **132**, 120–140.
743 Jones R. H., Mccubbin F. M., and Guan Y., (2016) Phosphate minerals in the H group of ordinary
744 chondrites, and fluid activity recorded by apatite heterogeneity in the Zag H5-8 regolith breccia.
745 *American Mineralogist* **323**, 4674–4689.

Kaplan H. H. Lauretta D. S., Simon A. A., Hamilton V. E., DellaGiustina D. N., Golish D. R., Reuter D. C., Bennett C. A., Burke K. N., Campins H., Connolly Jr. H. C., Dworkin J. P., Emery J. P., Glavin D. P., Glotch T. D., Hanna R., Ishimaru K., Jawin E. R., McCoy T. J., Porter N., Sandford S. A., Ferrone S., Clark B. E., Li J.-Y., Zou X.-D., Daly M. G., Barnouin O. S., Seabrook J. A. and Enos H. L. (2020) Bright carbonate veins on asteroid (101955) Bennu: Implications for aqueous alteration history. *Science*, **370**, eabc3557.

Kemper, F., Jager, C., Waters, L.B.F.M., Henning, T., Molster, F.J., Barlow, M.J., Lim, T. and de Koter, A. (2002) Detection of carbonates in dust shells around evolved stars. *Nature* **415**, 295-297.

Kerridge J. F., Mackay A. L. and Boynton W. V. (1979) Magnetite in CI carbonaceous meteorites - Origin by aqueous activity on a planetesimal surface. *Science* **205**, 395-397.

Krzesińska A. M. and Almeida N. V. (2019) Evidence of shock-induced vaporization of matrix to form porosity in Baszkowka, a porous L5 chondrite. *Meteorit. Planet. Sci.* **54**, 54-71.

Langenhorst F. (2002) Shock metamorphism of some minerals: Basic introduction and microstructural observations. *Bulletin of the Czech Geological Survey*, **77**, 265–282.

Langenhorst F. and Deutsch A. (2012) Shock metamorphism of minerals. *Elements* **8**, 31–36.

Langenhorst F., Shaw C. S. J. and Metzler K. (2000a) Mineral chemistry and microstructures in ALH 84001 (abstract #1866), *31st Lunar and Planetary Science Conference*.

Langenhorst F., Deutsch A., Ivano v B. A. and Honemann U. (2000b) On the shock behavior of $CaCO_3$: Dynamic loading and fast unloading experiments – modeling – mineralogical observations (abstract #1851), *31st Lunar and Planetary Science Conference*.

Larsson A. K. and Christy A. G. (2008) On twinning and microstructures in calcite and dolomite. *American Mineralogist* **93**, 103-113.

Latychevskaia T., Escher C. and Fink H.-W. (2019) Moiré structures in twisted bilayer graphene studied by transmission electron microscopy. *Ultramicroscopy* **197**, 46–52.

Lee M. R. and Ellen R. (2008) Aragonite in the Murray (CM2) carbonaceous chondrite: Implications for parent body compaction and aqueous alteration. *Meteorit. Planet. Sci.* **43**, 1219–1231.

Lee M. R., Lindgren P., Sofe M. R., Alexander C. M. O'D. and Wang J. (2012) Extended chronologies of aqueous alteration inthe CM2 carbonaceous chondrites: evidence from carbonates in Queen Alexandra Range 93005. *Geochim. Cosmochim. Acta* **92**, 148–169.

777 Lee M. R., Sofe M. R., Lindgren P., Starkey N. A. and Franchi I. A. (2013) The oxygen isotope
778 evolution of parent body aqueous solutions as recorded by multiple carbonate generations in
779 the Lonewolf Nunataks 94101 CM2 carbonaceous chondrite. *Geochim. Cosmochim. Acta* **121**,
780 452–466.
781 Lee M. R., Lindgren P. and Sofe M. R. (2014) Aragonite, breunnerite, calcite and dolomite in the
782 CM carbonaceous chondrites: High fidelity recorders of progressive parent body aqueous
783 alteration. *Geochim. Cosmochim. Acta* **144**, 126-156.
784 Leitner J., Vollmer C., Hoppe P. and Zipfel J. (2012) Characterization of presolar material in the
785 CR chondrite Northwest Africa 852. *The Astrophysical Journal* **745**, 38 (16pp).
786 Lewis J. A. and Jones R. H. (2016) Phosphate and feldspar mineralogy of equilibrated L
787 chondrites: The record of metasomatism during metamorphism in ordinary chondrite parent
788 bodies. *Meteorit. Planet. Sci.* **51**, 1886-1913.
789 Lisse C. M., Kraemer K. E., Nuth III J. A., Li A., and Joswiak D. (2007) Comparison of the
790 composition of the Tempel 1 ejecta to the dust in Comet C/Hale-Bopp 1995 O1 and YSO HD
791 100546. *Icarus* **187**, 69-86.
792 Lisse C. M., VanCleve J., Adams A. C., A'Hearn M. F., Fernandez Y. R., Farnham T. L., Armus
793 L., Grillmair C. J., Ingalls J., Belton M. J. S., Groussin O., McFadden L. A., Meech K. J.,
794 Schultz P. H., Clark B. C., Feaga L. M., Sunshine J. M. (2006) Spitzer spectral observations of
795 the Deep Impact ejecta. *Science* **313**, 635-640.
796 Litasov K. D., Bekker T. B., Sagatov N. E., Gavryushkin P. N., Krinitsyn P.G. and Kuper K. E.
797 (2020) $(Fe,Ni)_2P$ allabogdanite can be an ambient pressure phase in iron meteorites. *Scientific*
798 *Reports* **10**, 8956.
799 Love S. G. and Brownlee D. E. (1993) A direct measurement of the terrestrial mass accretion rate
800 of cosmic dust. *Science* **262**, 550–553.
801 Martin C., Debaille V., Lanari P., Goderis S., Vandendael I., Vanhaecke F., Vidal O. and Claeys
802 P. (2013) REE and Hf distribution among mineral phases in the CV–CK clan: A way to explain
803 present-day Hf isotopic variations in chondrites. *Geochim. Cosmochim. Acta* **120**, 496-513.
804 Martinez I., Deutsch A., Schärer U., Ildefonse P., Guyot F. and Agrinier P. (1995) Shock recovery
805 experiments on dolomite and thermodynamical calculations of impact induced decarbonation.
806 *Journal of Geophysical Research* 100, 15465-15476.

Metzler K., Bischoff A. and Stoeffler D. (1992) Accretionary dust mantles in CM chondrites: Evidence for solar nebula processes. *Geochim. Cosmochim. Acta* **56**, 2873-2897.

Miser D. E., Swinnea J. S. and Steinfink H. (1987) TEM observations and X-ray crystal-structure refinement of a twinned dolomite with a modulated microstructure. *American Mineralogist* **72**, 188-193.

Mittlefehldt D. W. (1994) ALH 84001, a cumulate orthopyroxenite member of the Martian meteorite clan. *Meteoritics* **29**, 214-221.

Nicolas A. and Poirier J. P. (1976) Crystalline plasticity and solid state flow in metamorphic rocks. Wiley, New York, 444 pp.

Noguchi T., Nakamura T. and Nozaki W. (2002) Mineralogy of phyllosilicate-rich micrometeorites and comparison with Tagish Lake and Sayama meteorites. *Earth and Planetary Science Letters* **202**, 229–246.

Noguchi T., Yabuta H., Itoh S., Sakamoto N., Mitsunari T., Okubo A., Okazaki R., Nakamura T., Tachibana S., Terada K., Ebihara M., Imae N., Kimura M. and Nagahara H. (2017) Variation of mineralogy and organic material during the early stages of aqueous activity recorded in Antarctic micrometeorites. *Geochim. Cosmochim. Acta* **208**, 119–144.

Ogliore R. C., Liu N., Dobrică E., Donohue P. H., Jilly-Rehak C. E., Duprat J., Engrand C. and Brearley A. J. (2019) ^{53}Mn-^{53}Cr radiometric dating of secondary carbonates in a hydrated Antarctic micrometeorite. (abstract #2132), *50th Lunar and Planetary Science Conference*.

Osinski G. R., Spray J. G. and Grieve R. A. F. (2008) Impact melting in sedimentary target rocks: An assessment. In *The sedimentary record of meteorite impacts*, edited by Evans K. R., Horton J. W., King D. T., and Morrow J. R. Geological Society of America Special Paper **437**,1–17.

Oze C. and Sharma M. (2007) Serpentinization and the inorganic synthesis of H_2 in planetary surfaces. *Icarus* **186**, 557-561.

Petitat M., Marrocchi Y., McKeegan K. D., Mostefaui S., Meibom A., Zolensky M. E. and Gounelle M. (2011) ^{53}Mn-^{53}Cr ages of Kaidun carbonates. *Meteorit. Planet. Sci.* **46**, 275–283.

Post J. E. (1999) Manganese oxide minerals: crystal structures and economic and environmental significance. *Proc. Natl. Acad. Sci.* **96**, 3447–3454.

Reeder R. J. and Wenk H. R. (1979) Microstructures in low temperature dolomites. *Geophysical Research Lett.* **6**, 77-80.

837 Reeder R. J. (1992) Carbonates: Growth and alteration microstructures. In: Minerals and Reaction
838 at the Atomic Scale: Transmission Electron Microscopy (P. Busek, editor). Reviews in
839 Mineralogy, 27. Mineralogical Society of America, Washington, D.C., pp. 381-424.
840 Reidy K., Varnavides G., Thomsen J. D., Kumar A., Pham T., Blackburn A. M., Anikeeva P.,
841 Narang P., LeBeau J. M. and Ross F. M. (2021) Direct imaging and electronic structure
842 modulation of moiré superlattices at the 2D/3D interface. *Nat Commun* **12**, 1290.
843 Reksten K. (1990) Superstructures in calcian ankerites. *Physics and Chemistry of Minerals* **17**,
844 266-270.
845 Riciputi L. R., McSween H. Y., Johnson C. A. and Prinz M. (1994) Minor and trace element
846 concentrations in carbonates of carbonaceous chondrites, and implications for the compositions
847 of co-existing fluids. *Geochim. Cosmochim. Acta* **58**, 1343-1351.
848 Rietmeijer F. J. M. (1990). Salts in two chondritic porous interplanetary dust particles. *Meteoritics*
849 **25**, 209.
850 Rodriguez-Navarro C. and Ruiz-Agudo E. (2013) Carbonates: An overview of recent TEM
851 research. In *Minerals at the Nanoscale*, European Mineralogical Union, Notes in Mineralogy,
852 (editors Nieto F. and Livi K. J. T.), 14, chapter 10, 337-375.
853 Rowe M. W., Clayton R. N. and Mayeda T. K. (1994) Oxygen isotopes in separated components
854 of CI and CM meteorites. *Geochim. Cosmochim. Acta* **58**, 5341-5347.
855 Rubin A. E., Keil K. and Scott E. R. D. (1997) Shock metamorphism of enstatite chondrites.
856 *Geochim. Cosmochim. Acta* **61**, 847–858.
857 Rubin A. E. and Ma C. (2017) Meteoritic minerals and their origins. *Chemie der Erde -*
858 *Geochemistry*, **77**, 325-385.
859 Ruzicka A., Killgore M., Mittlefehldt D.W. and Fries, M.D. (2005) Portales Valley: Petrology of
860 a metallic-melt meteorite breccia. *Meteorit. Planet. Sci.* **4**, 261–295.
861 Sakamoto K., Nakamura T., Noguchi T., and Tsuchiyama A. (2010) A new variant of saponite-
862 rich micrometeorites recovered from recent Antarctic snowfall. *Meteorit. Planet. Sci.* **45**, 220–
863 237.
864 Sandford S. A. and Walker R. M. (1985) Laboratory infrared transmission spectra of individual
865 interplanetary dust particles from 2.5 to 25 microns. *The Astrophysical Journal* **291**, 838–851.
866 Schramm L. S., Brownlee D. E., and Wheelock M. M. (1989) Major element composition of
867 stratospheric micrometeorites. *Meteoritics* **24**, 99-112.

Schulte M. and Shock E. (2004) Coupled organic synthesis and mineral alteration on meteorite parent bodies. *Meteorit. Planet. Sci.* **39**, 1577–1590.

Scott E. R. D., Keil K. and Stöffler D. (1992) Shock metamorphism of carbonaceous chondrites. *Geochim. Cosmochim. Acta* **56**, 4281–4293.

Shukolyukov A. and Lugmair G. (2006) Manganese-chromium isotope systematics of carbonaceous chondrites. *Earth Planet. Sci. Lett.* **250**, 200–213.

Sirohi R. S. and Chau F. S. (1999) Optical Methods of Measurement - Wholefield Techniques, Marcel Dekker, Inc., New York, (1999).

Sleep N. H., Meibom A., Fridriksson T., Coleman R. G., and Bird D. K. (2004) H_2-rich fluids from serpentinization: Geochemical and biotic implications. *P Natl Acad Sci USA* **101**, 12818-12823.

Stöffler D., Keil K., and Scott E. R. D. (1991) Shock metamorphism in ordinary chondrites. *Geochim. Cosmochim. Acta* **55**, 3845–3867.

Suttle M. D., Genge M. J. and Russell, S.S. (2017) Shock fabrics in fine-grained micrometeorites. *Meteorit. Planet. Sci.* **52**, 2258-2274.

Telus M., Alexander C. M. O'D., Hauri E. H. and Wang J. (2019) Calcite and dolomite formation in the CM parent body: Insight from in situ C and O isotope analyses. *Geochim. Cosmochim. Acta* **175**, 275-291.

Theocaris P. S. (1969) Moiré Fringes in Strain Analysis. Chapter 1 - General Theory. The Commonwealth and International Library: Applied Mechanics Division, Publisher Pergamon, pp 1-18.

Tomeoka K. and Buseck P. R. (1986) A carbonate-rich, hydrated, interplanetary dust particle: Possible residue from protostellar clouds. *Science* **231**, 1544–1546.

Toppani A., Robert F., Libourel G., de Donato P., Barres O., D'Hendecourt L., Ghanbaja J., (2005) A `dry' condensation origin for circumstellar carbonates. *Nature* **437**, 1121-1124.

Treiman A. H. (1995) A petrographic history of Martian meteorite ALH 84001: Two shocks and an ancient age. *Meteoritics* **30**, 294-302.

Treiman A. H., Gleason J. D. and Bogard D. D. (2000) The SNC meteorites are from Mars. *Planetary and Space Science* **48**, 1213-1230.

Tyra M., Farquharb J., Guanc Y. and Leshind L. A. (2012) An oxygen isotope dichotomy in CM2 chondritic carbonates—A SIMS approach. *Geochim. Cosmochim. Acta* **77**, 383–395.

Tyra M. A. (2013) Using oxygen and carbon stable isotopes, ^{53}Mn–^{53}Cr isotope systematics, and petrology to constrain the history of carbonates and water in the CR and CM chondrite parent bodies. Ph. D. Thesis, University of New Mexico.

Tyra M., Brearley A. and Guan Y. (2016) Episodic carbonate precipitation in the CM chondrite ALH 84049: An ion microprobe analysis of O and C isotopes. *Geochim. Cosmochim. Acta* **175**, 195–207.

Tucker, M. and Wright, V.P. (1990) Carbonate Sedimentology. Blackwell Scientific Publications, Oxford, pp 482.

Vacher L. G., Piralla M., Gounelle M., Bizzarro M. and Marrocchi Y. (2019) Thermal evolution of hydrated asteroids inferred from oxygen isotopes. *The Astrophysical Journal Lett.* **882**, L20, 8 pp.

Van Kooten E. M. M. E., Wielandt D., Schiller M., Nagashima K., Thomen A., Larsen K. K., Olsen M. B., Nordlund Å., Krot A. N. and Bizzarro M. (2016) Isotopic evidence for primordial molecular cloud material in metal-rich carbonaceous chondrites. *PNAS* **113**, 2011-2016.

Verdier-Paolettia M. J., Marrocchi Y., Avice G., Roskosz M., Gurenko A. and Gounelle M. (2017) Oxygen isotope constraints on the alteration temperatures of CM chondrites. *Earth Planet. Sci. Lett.* **458**, 273–281.

Wada K., Grott M., Michel P., Walsh K. J., Barucci A. M., Biele J., Blum J., Ernst C. M., Grundmann J. T., Gundlach B., Hagermann A., Hamm M., Jutzi M., Kim M.-J., Kührt E., Corre L., Libourel G., Lichtenheldt R., Maturilli A., Messenger S. R., Michikami T., Miyamoto H., Mottola S., Müller T., Nakamura A. M., Nittler L. R., Ogawa K., Okada T., Palomba E., Sakatani N., Schröder S. E., Senshu H., Takir D., Zolensky M. E. and International Regolith Science Group (IRSG) in Hayabusa2 project (2018) Asteroid Ryugu before the Hayabusa2 encounter. *Progress in Earth and Planetary Science* **5**, 82.

Wang S. L. (1992) An introduction to Moiré method. TH Eindhoven. Afd. Werktuigbouwkunde, Vakgroep Produktietechnologie : WPB; Vol. WPA1278). Technische Universiteit Eindhoven.

Wang Q., Ri S., Tsuda H. and Tokizaki T. (2015) Deformation measurement method using moiré fringes at high scanning speed under a laser scanning microscope. Optics. Special Issue: Optical Techniques for Deformation, Structure and Shape Evaluation. **4**, 43-49.

Ward D., Bischoff A., Roszjar J., Berndt J. and Whitehouse M. J. (2017) Trace element inventory of meteoritic Ca-phosphates. *American Mineralogist* **102**, 1856–1880.

Warren J. (2000) Dolomite: Occurrence, evolution and economically important associations *Earth-Science Reviews* **52**, 1–81.

Weisberg M. K., Prinz M., Clayton R. N. and Mayeda T. K. (1993) The CR (Renazzo-type) carbonaceous chondrite group and its implications. *Geochim. Cosmochim. Acta* **57**, 1567–1586.

Yada T., Abe M., Okada T., Nakato A., Yogata K., Miyazaki A., Hatakeda K., Kumagai K., Nishimura M., Hitomi Y., Soejima H., Yoshitake M., Iwamae A., Furuya S., Uesugi M., Karouji Y., Usui T., Hayashi T., Yamamoto D., Fukai R., Sugita S., Cho Y., Yumoto K., Yabe Y., Bibring J.-P., Pilorget C., Hamm V., Brunetto R., Riu L., Lourit L., Loizeau D., Lequertier G., Moussi-Soffys A., Tachibana S., Sawada H., Okazaki R., Takano Y., Sakamoto K., Miura Y., Yano H., Ireland T., Yamada T., Fujimoto M., Kitazato K., Namiki N., Arakawa M., Hirata N., Yurimoto H., Nakamura T., Noguchi T., Yabuta H., Naraoka H., Ito M., Nakamura E., Uesugi K., Kobayashi K., Michikami T., Kikuchi H., Hirata N., Ishihara Y., Matsumoto K., Noda H., Noguchi R., Shimaki Y., Ogawa K., Shirai K., Wada K., Senshu H., Yamamoto Y., Morota T., Honda R., Honda C., Yokota Y., Matsuoka M., Sakatani N., Tatsumi E., Miura A., Yamada M., Fujii A., Hirose C., Hosoda S., Ikeda H., Iwata T., Kikuchi S., Mimasu Y., Mori O., Ogawa N., Ono G., Shimada T., Soldini S., Takahashi T., Takei Y., Takeuchi H., Tsukizaki R., Yoshikawa K., Terui F., Nakazawa S., Tanaka S., Saiki T., Yoshikawa M., Watanabe S.-I., and Tsuda Y. (2021) Ryugu: A brand-new planetary sample returned from a C-type asteroid. 10.21203/rs.3.rs-608561/v1.

Zolensky M. E. and Lindstrom D. J. (1992) Mineralogy of 12 large "chondritic" interplanetary dust particles. *22nd Lunar and Planetary Science Conference Proceedings*. pp. 161–169.

Zolensky M. E., Barrett R. and Browning L. (1993) Mineralogy and composition of matrix and chondrule rims in carbonaceous chondrites. *Geochim. Cosmochim. Acta* **57**, 3123–3148.

Zolensky M. E., Mittlefehldt D. W., Lipschutz M. E., Wang M.-S., Clayton R. N., Mayeda T. K., Grady M. M., Pillinger C., David B., (1997) CM chondrites exhibit the complete petrologic range from type 2 to 1. *Geochim. Cosmochim. Acta* **61**, 5099-5115.

Zolensky M., Nakamura-messenger K., Rietmeijer F., Leroux H., Mikouchi T., Ohsumi K., Simon S., Grossman L., Stephan T., Weisberg M., Velbel M., Zega T., Stroud R., Tomeoka K., Ohnishi I., Tomioka N., Nakamura T., Matrajt G., Joswiak D., Brownlee D., Langenhorst F., Krot A., Kearsley A., Ishii H., Graham G., Dai Z. R., Chi M., Bradley J., Hagiya K., Gounelle M. and

Bridges J. (2008) Comparing Wild 2 particles to chondrites and IDPs. *Meteorit. Planet. Sci.* **43**, 261–272.

FIGURE CAPTIONS

Figure 1. Backscattered electron (BSE) micrographs of the Antarctic micrometeorite (AMM, 03-36-46) analyzed in this study showing the external surface (a) and the polished surface (b) of the entire particle collected from the pristine Concordia snow. The white arrows (b) show the location of the secondary ion mass spectrometer (SIMS) analyses that were carried out in the magnetite-dolomite assemblage (Dobrică et al. 2019). c-f) Detailed BSE images of the regions of interest highlighted by the white dashed line squares (b). Focused ion beam (FIB) sections prepared for transmission electron microscopy (TEM) studies are shown as white solid line rectangles. The carbonates (Carb) are located in two regions (c - region A, FIB section UH-001, and f - region B, FIB section UH-002). Two other FIB sections (d - UH-003; e - UH-006) were prepared in the remaining material. Phases identified in the secondary electron microscope (SEM) images using energy-dispersive X-ray spectroscopy (EDS): carb - carbonates, mt - magnetite, P - phosphate, S - sulfide.

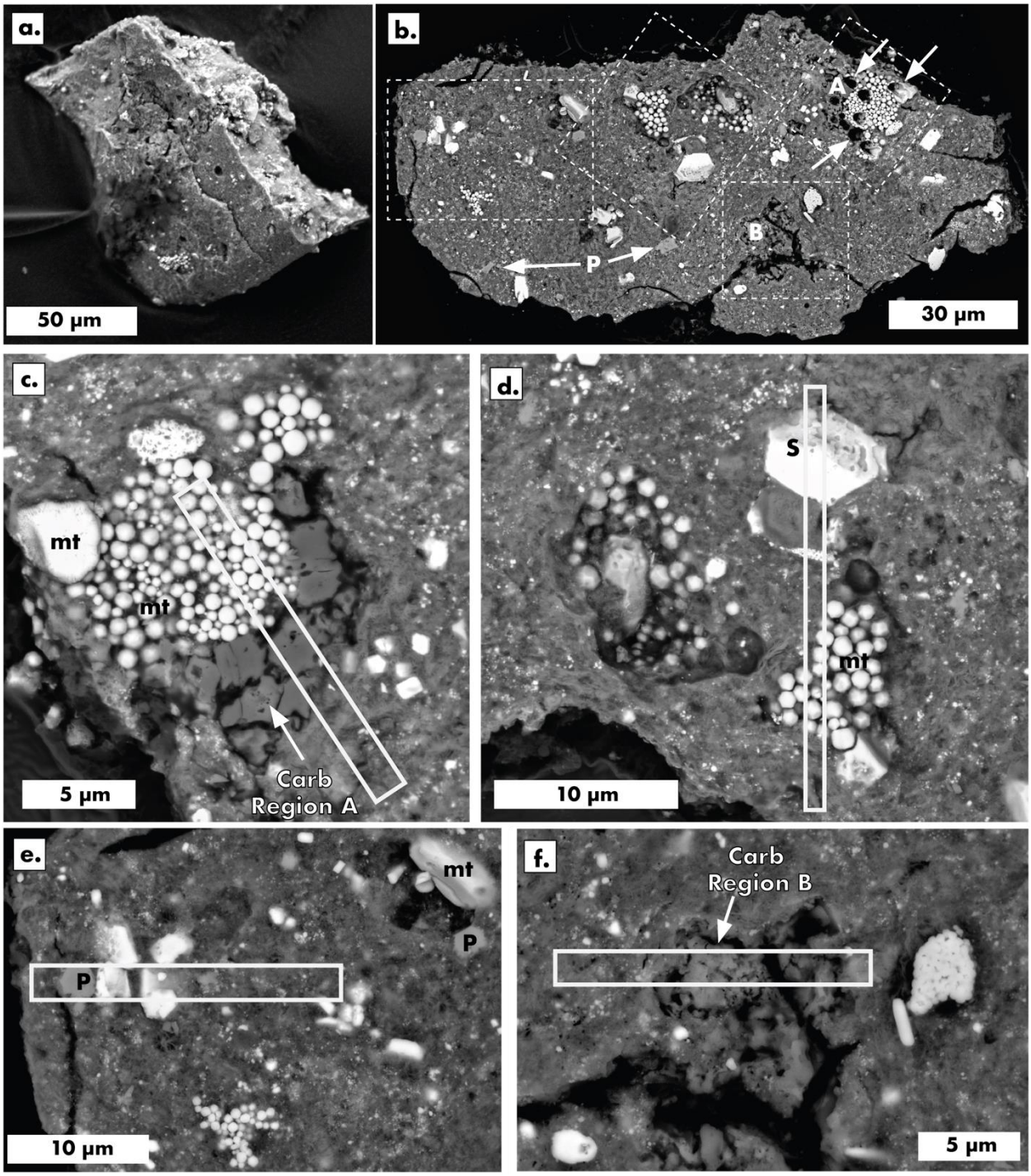
a.
50 µm
b.
A
B
P
30 µm
c.
mt
mt
Carb
Region A
5 µm
d.
S
mt
10 µm
e.
mt
P
P
10 µm
f.
Carb
Region B
5 µm

974

975

Figure 2. Dark-field (a, c) micrographs and energy dispersive X-ray (EDS) maps (b, d-e) made by scanning transmission electron microscopy (STEM) showing the texture and the chemical composition of the carbonates identified in region A (a-b) and region B (c-e). The white rectangle (a) shows the region where the EDS map of C, Mn, and Fe was made. This composite EDS map shows the distribution of carbonates (Dol), C-rich amorphous material (C-rich am), and sulfides (S). Additionally, we show the manganese (d) and iron (e) EDS maps of the carbonate cluster from region B highlighted by the white, rectangle, dashed line shown in (c). Phases identified in the TEM images using energy-dispersive X-ray spectroscopy (EDS): C-rich am - C-rich amorphous material, dol - dolomite, Ank : ankerite, f-g phyllo - fine-grained phyllosilicates, mt - magnetite, and S - sulfide.

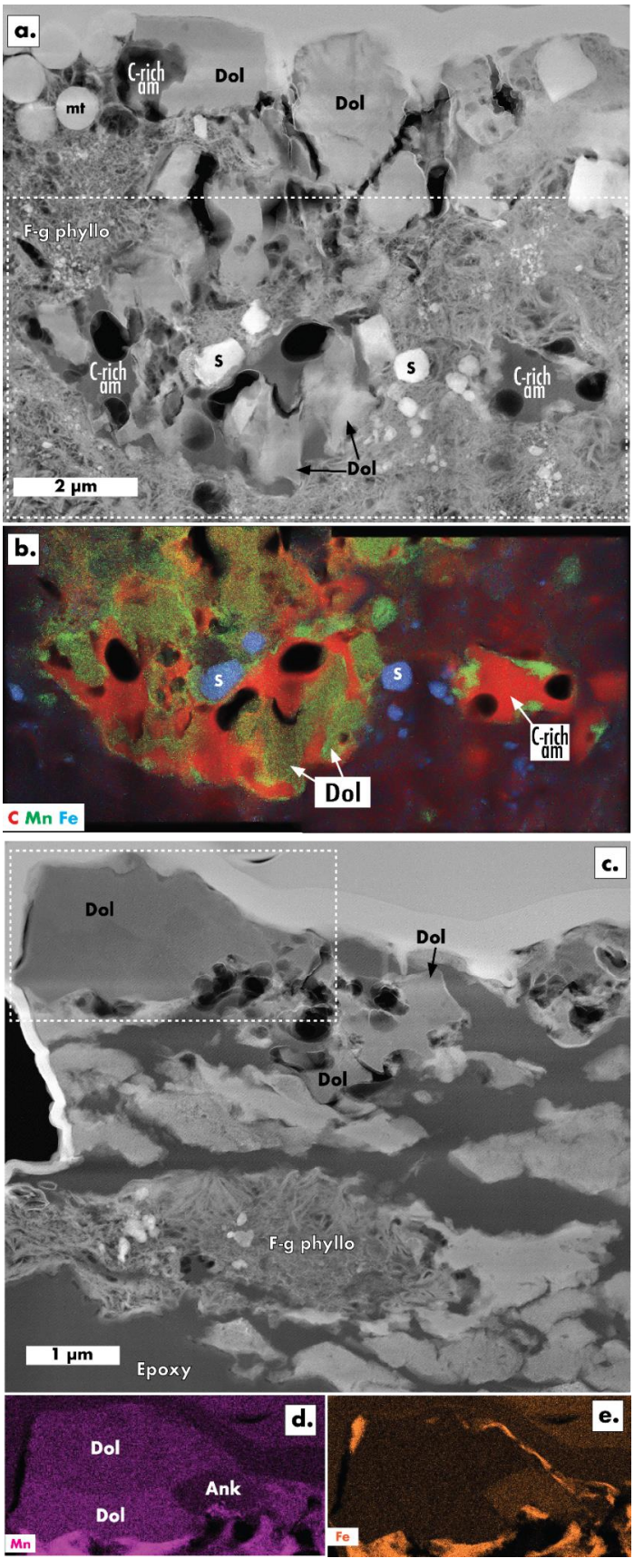
a.
C-rich am
Dol
mt
Dol
F-g phyllo
C-rich am
S
S
C-rich am
Dol
2 µm
b.
S
S
C-rich am
Dol
C Mn Fe
c.
Dol
Dol
Dol
F-g phyllo
1 µm
Epoxy
d.
Dol
Ank
Dol
Mn
e.
Fe

986

Figure 3. a-b) Ternary diagram [$MgCO_3$-$CaCO_3$-$(Fe+Mn)CO_3$, in mole%] and an enlarged region of the ternary diagram indicated by the shaded area (a) showing the compositions of the carbonates in region A (UH-001, dolomite - grey triangles) and region B (UH-002, dolomite - left crystal, top, LT - white diamond; left crystal, bottom, LB - white circles; right crystal, top, RT - light grey polygon; ankerite - right crystal, bottom, RB - light grey square, see Fig. 5 to locate these regions). For comparison, we plotted the data for ALH 84001 (black squares, Mittlefehldt 1994; Brearley 2003), CM chondrites (brown area, Tyra 2013; Zolensky et al. 1997; Lee et al. 2012), and CI chondrites (black dashed line, Petitat et al. 2011). c) $MnCO_3$ versus $CaCO_3$ (mol%) of dolomite compositions measured in both regions A and B compared with CI chondrites (‡, Endreß and Bishoff 1996; Johnson and Prinz 1993), CM chondrites (‡‡, Tyra et al. 2016), and Tagish Lake (‡‡‡, C2-ung; Blinova 2013). Plotted are the Ca deficiencies in dolomites from CI chondrites (Alais, Ivuna, and Orgueil from ‡Endreß and Bishoff 1996) reflecting lower formation temperatures than those described by Goldsmith and Graf (1960) in terrestrial dolomites.

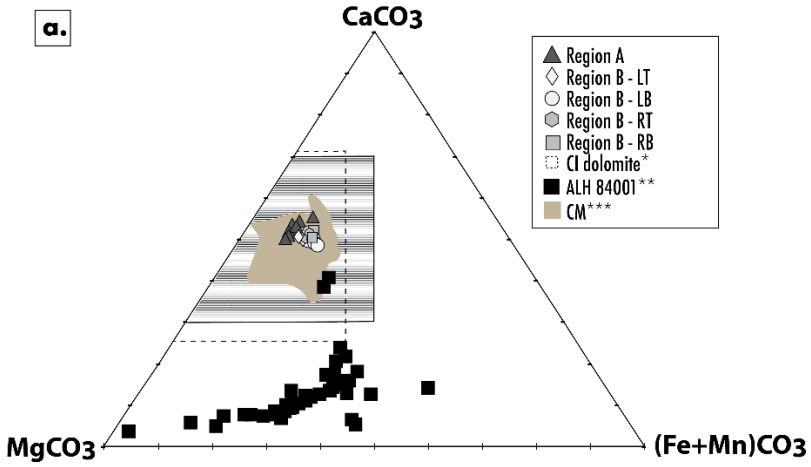
a.
CaCO3
MgCO3
(Fe+Mn)CO3
Region A
Region B - LT
Region B - LB
Region B - RT
Region B - RB
CI dolomite*
ALH 84001**
CM***

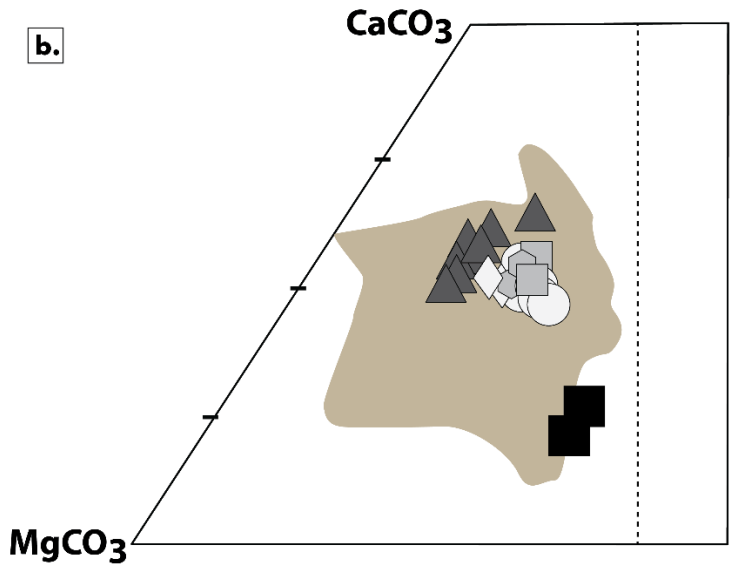
b.
CaCO3
MgCO3

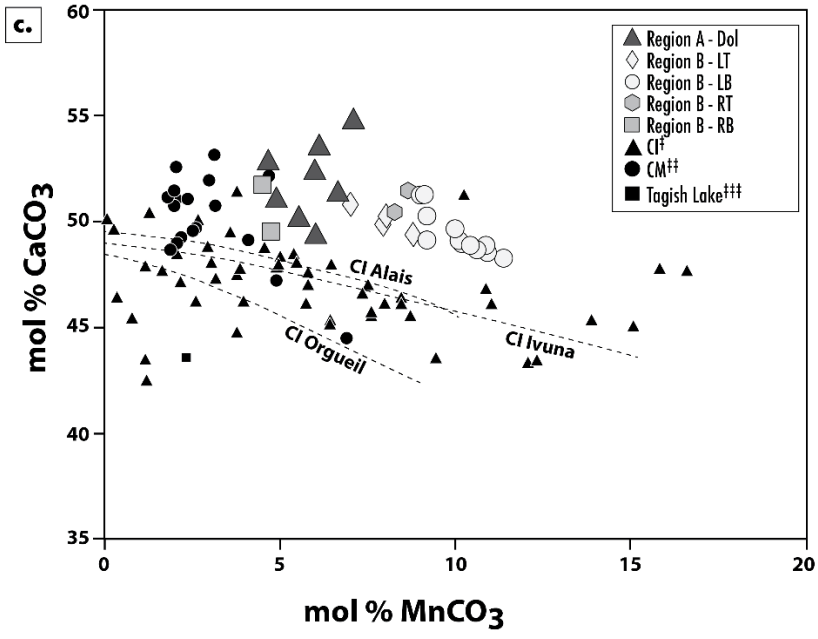
c.
mol % CaCO3
mol % MnCO3
60
55
50
45
40
35
0
5
10
15
20
CI Alais
CI Orgueil
CI Ivuna
Region A - Dol
Region B - LT
Region B - LB
Region B - RT
Region B - RB
CI‡
CM‡‡
Tagish Lake‡‡‡

1000

Figure 4. Dark- (a) and bright-field (b-c) scanning transmission electron microscopy (STEM) micrographs showing the texture of the dolomite (dol) crystals identified in region A. c-d) Detailed bright-field micrographs of the regions of interest highlighted by the black squares (b - dashed line; c - solid line) showing the presence molulations (b - parallel lamellae alternating dark/light contrast), pores (c - withe arrows), and ion beam damaged top surface (~ 450 nm in thickness, white dashed line) produced during the NanoSIMS measurements (Ogliore et al. 2019). The pores have sizes up to ~90 nm in diameter.

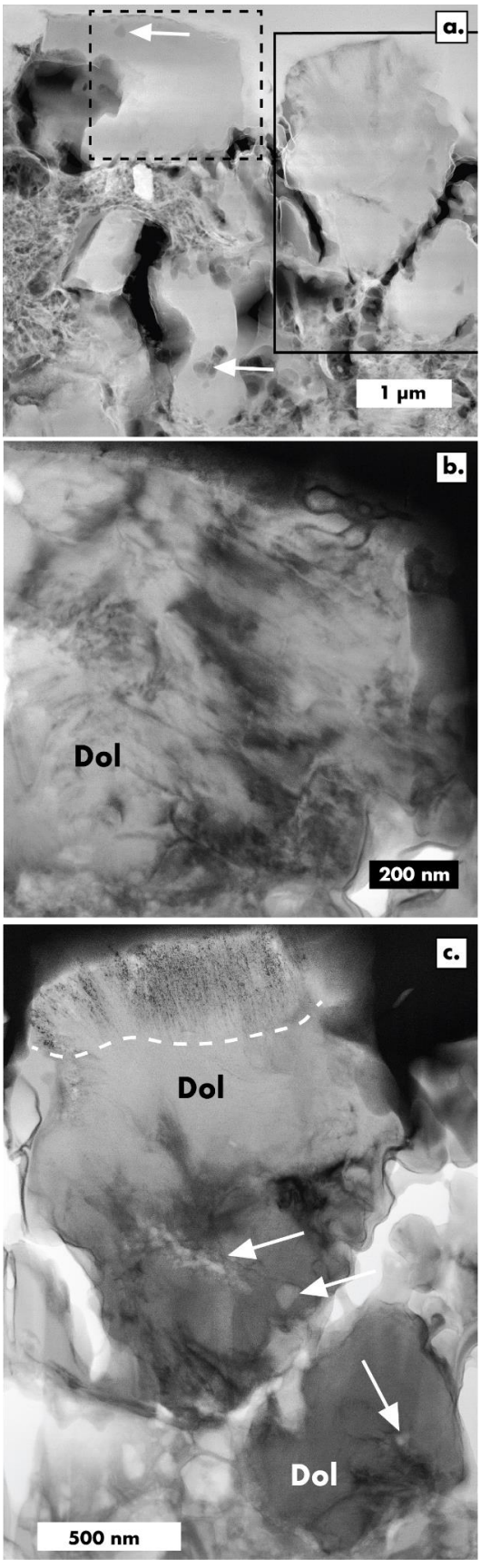

1009

Figure 5. Detailed transmission electron microscopy (TEM, a, d, e, g, i, j) micrographs, energy dispersive (EDS) X-ray maps (b, c, f), and fast Fourier transform (FFT) diffraction pattern (h) showing the complex microstructure and chemical composition (Fe and Mn) of a cluster of dolomite (dol, LT - left crystal, top part; LB - left crystal, bottom part; RT - right crystal, top part) and ankerite (ank, RB - right crystal, bottom part) crystals from the hydrated fine-grained Antarctic micrometeorite (H-FgMMs, 03-36-46) that was analyzed in this study. Different TEM modes were used to obtained these micrographs such as bright-field (BF, a) and high-resolution (HR, g, i, j) TEM mode and nanodiffraction (d-e, convergence angle of 0.1–0.3 mrad) in scanning transmission electron microscopy (STEM) mode. For diffraction, we used both selected area electron diffraction (SAED, d) and FFT of HRTEM images (g-j). The carbonate cluster is composed of two zoned crystals (a) of dolomite and ankerite with different crystallographic orientations. The Fe and Mn maps of the white box outlined in (a) are shown in (b-c). These EDS maps show the Fe and Mn zonation of the ankerite (see white dashed line separating the Fe-poor top of the ankerite crystal from the bottom Fe-rich. Note Fe-rich inclusions in the left dolomite crystals (b - white arrows). The dolomite crystal is also zoned (d-f). Bright-field (BF) STEM and EDS map (d-f) of manganese showing the Mn variation in the dolomite. We observe heterogeneity in the distribution of manganese in the bottom area of the crystal. The heterogeneities (f, black arrows) could correspond to the modulations shown in (d). These modulations appear as parallel lamellae alternating dark/light contrast. High-resolution TEM images of (g, i, j) moiré fringes (g, j) at the grain boundary between ankerite and dolomite and the modulation (i) in the center of the dolomite crystal. Fast Fourier Transform (FFT) patterns of the HR images are shown (g, h, i, j). The FFTs show the pattern resulting from the moiré structure (h) and the ankerite crystal close to the interface (g - bottom), and the modulation structure (i). Note streaking in the $\bar{1}32\bar{4}$ direction (i), which generally appear in carbonates showing modulated structures. This moiré FFT pattern (h) exhibits peaks originating from the two lattices and the moiré peaks. Two FFTs stacks (red - top and green - bottom) of the ankerite and dolomite identified on each side of the boundary contain the moiré structure. The two crystals show an orientation mismatch (j) of a relative rotation angle of ~4° between lattice fringes.

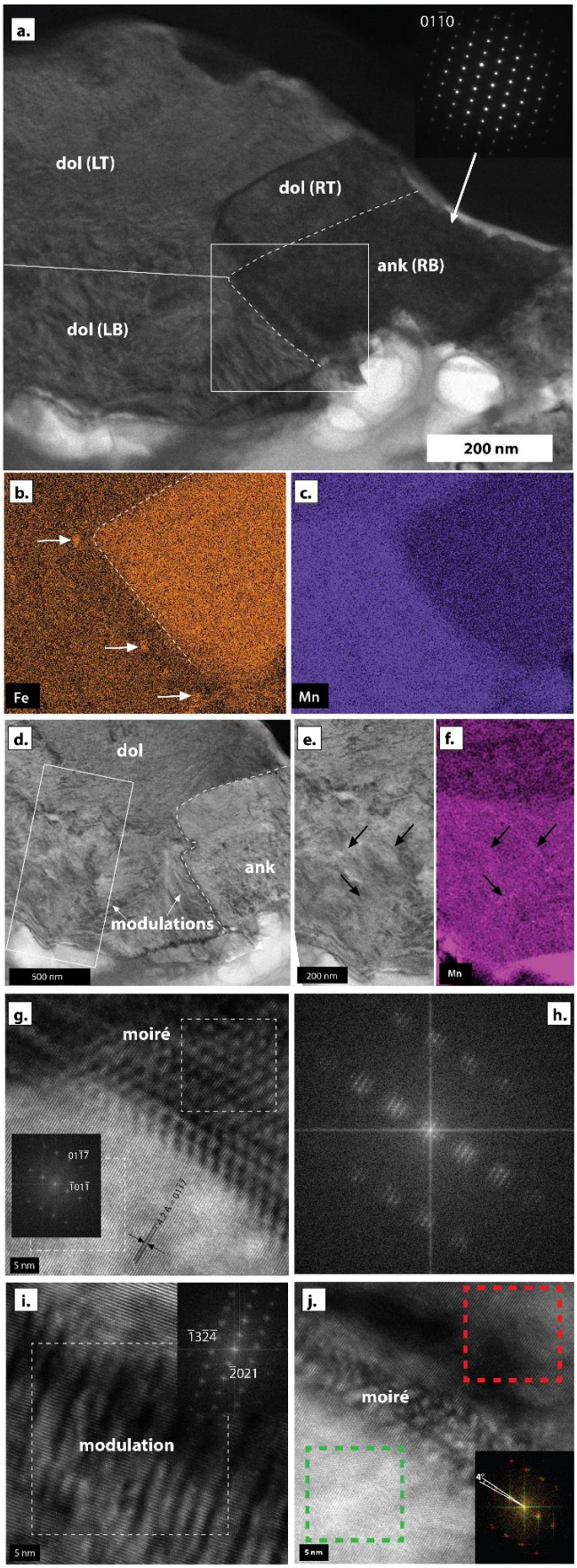
a.
0110
dol (LT)
dol (RT)
ank (RB)
dol (LB)
200 nm
b.
Fe
c.
Mn
d.
dol
ank
modulations
500 nm
e.
200 nm
f.
Mn
g.
moiré
5 nm
h.
i.
modulation
5 nm
j.
moiré
5 nm

Figure 6. Detailed dark-field (a-d) and bright-field (e-f) scanning transmission electron microscopy (DF- and BF-STEM) micrographs showing the minerals associated with carbonates in the analyzed hydrated fine-grained Antarctic micrometeorite (03-36-46). Several minerals were identified such as coarse- and fine-grained phyllosilicates (a-f), magnetite (c), sulfide (a-b, d, f), barringerite (b), and Ca-phosphate (e-f). Additionally, a S-rich (7 wt% SO_3) region of compact phyllosilicates (b, white dashed line) was identified in contact with micrometer-sized, Ni-poor sulfides. Most of these micrometer-sized sulfides show irregular edges with embayments (b, d) up to ~340 µm long. Furthermore, nanometer-sized, Ni-poor sulfides (a, white arrows) are found embedded in the fine-grained phyllosilicate matrix. Magnetite with two different morphologies (framboidal and radial) are shown in (c). Detailed BF-STEM images showing the presence of Ca-phosphates (e-f) containing irregular pores (white arrows). Two selected area electron diffraction (SAED) patterns were indexed as [001] (c) and [$1\bar{3}2$] (e) zone axis of magnetite and apatite, respectively. Phases identified in the STEM micrographs using energy-dispersive X-ray spectroscopy (EDS) and SAED: barr - barringerite, C-g phyllo - coarse-grained phyllosilicates, f-g phyllo - fine-grained phyllosilicates, mt - magnetite, P - Ca-phosphate (apatite), S - sulfide.

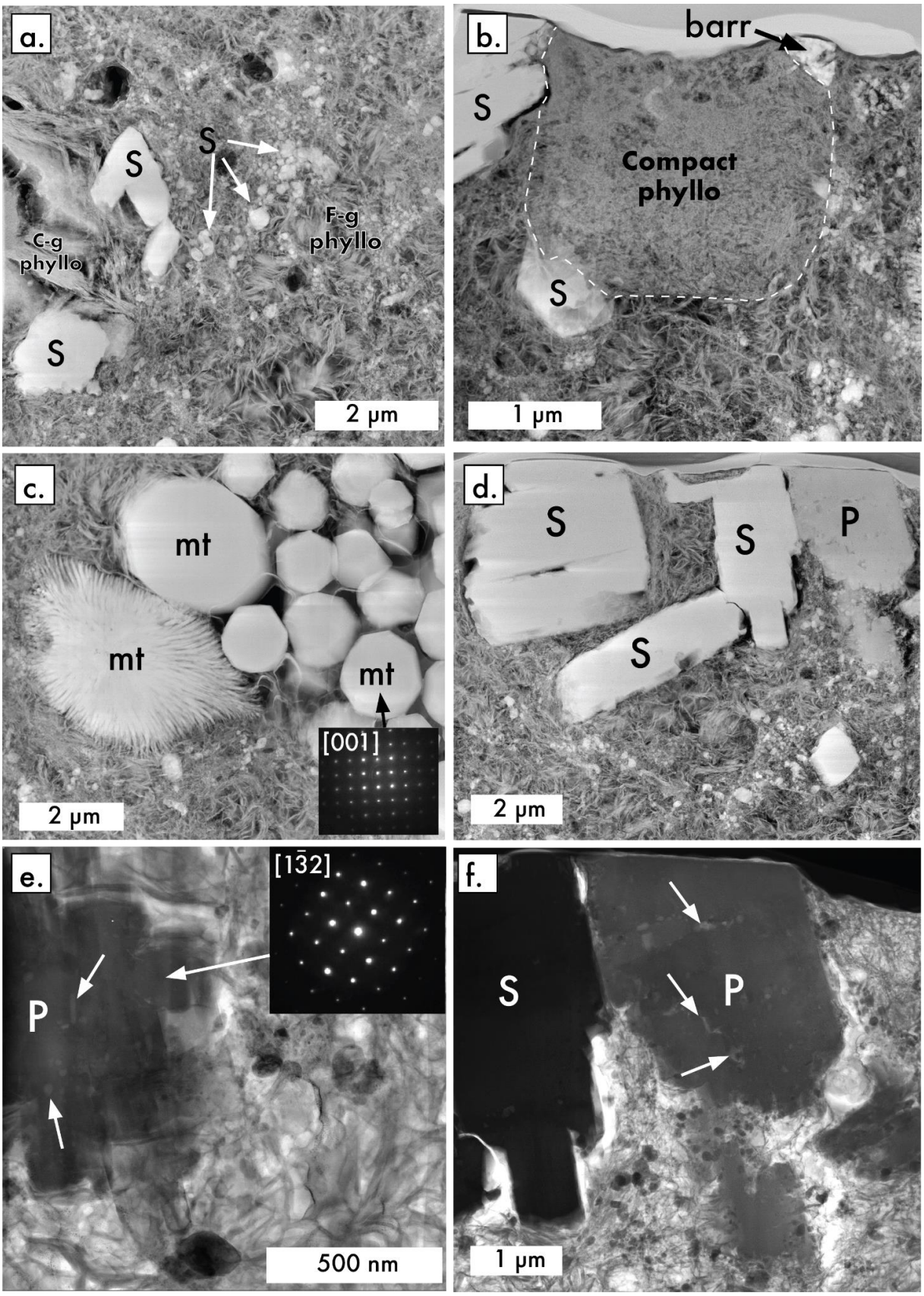
a.
S
S
S
C-g phyllo
F-g phyllo
S
2 µm
b.
barr
S
Compact phyllo
S
1 µm
c.
mt
mt
mt
[001]
2 µm
d.
S
S
P
S
2 µm
e.
[1$\bar{3}$2]
P
500 nm
f.
S
P
1 µm

1055

Table 1. Major and minor element compositions (in atom % and wt% oxide) determined by energy-dispersive X-ray spectroscopy of carbonates from region A and B, Ca-phosphate and coarse-grained and fine-grained phyllosilicates. The location of the carbonates is indicated in Figure 5 (LT - left crystal, top; LB - left crystal, bottom; RT - right crystal, top; RB - right crystal, bottom).

	Carbonates										**Ca-phosphates**		**Phyllosilicates**						
	Region A (UH-001)		**Region B (UH-002)**								**UH-001**	**UH-003**	**UH-001 F-g**		**UH-003 C-g**		**UH-003 F-g**	**UH-006 compact**	**UH-006 F-g**
			LT		**LB**		**RT**		**RB**										
N	**8**	**S.D.**	**4**	**S.D.**	**11**	**S.D.**	**2**	**S.D.**	**2**	**S.D.**	**1**	**1**	**6**	**S.D.**	**2**	**S.D**	**1**	**1**	**1**
wt%																			
SiO_2													53.6	3.3	39.9	1.0	52.2	43.6	50.2
Al_2O_3													2.2	2.5	3.7	0.0	4.6	5.5	5.9
Cr_2O_3													0.9	0.6	2.7	0.0	0.0	2.2	0.5
FeO	2.6	0.4	2.8	0.2	2.8	0.2	2.6	0.0	5.8	0.3	3.7	1.2	15.6	4.0	26.5	0.4	16.0	20.9	12.0
MnO	4.1	0.7	5.6	0.5	7.0	0.6	5.7	0.3	3.0	0.2			1.2	1.5	0.4	0.1	0.6	1.0	0.6
MgO	15.2	1.1	15.1	0.5	14.2	0.4	14.0	0.1	13.2	0.6			25.7	3.7	21.4	0.6	25.1	18.0	27.8
CaO	28.6	2.2	27.5	0.7	26.5	0.9	27.0	0.7	25.8	0.3	50.6	55.3	0.6	0.6	0.2	0.3	1.6	1.7	1.1
SO_3													0.0	0.0	5.3	0.4	0.0	7.0	1.8
P_2O_5											45.6	43.5							
CO_2	49.5	3.4	49.1	1.1	49.6	1.5	50.7	0.8	52.3	0.8									

Total											100	100	100		100		100	100	100
Mg/Fe	10.5		9.8		9.2		9.7		4.0										
at%																			
Si													15.1	0.9	11.6	0.3	14.9	12.7	14.2
Al													0.8	0.8	1.3	0.0	1.5	1.9	2.0
Cr													0.2	0.1	0.6	0.0	0.0	0.5	0.1
Fe	0.7	0.1	0.7	0.0	0.7	0.0	0.7	0.0	1.5	0.1	1.6	0.6	3.7	0.9	6.4	0.1	3.8	5.1	2.9
Mn	1.1	0.2	1.5	0.1	1.9	0.2	1.5	0.1	0.8	0.0			0.3	0.4	0.1	0.0	0.1	0.2	0.1
Mg	7.1	0.6	7.0	0.3	6.6	0.2	6.5	0.0	6.1	0.3			10.8	1.6	9.2	0.2	10.7	7.8	11.8
Ca	9.6	0.9	9.2	0.3	8.9	0.3	9.0	0.3	8.5	0.1	28.3	34.3	0.2	0.2	0.1	0.1	0.5	0.5	0.3
S													0.3	0.5	1.2	0.1	0.0	1.5	0.4
P											20.1	21.3							
O	60.5		60.5	0.2	60.6	0.2	60.8	0.1	61.0	0.1	50.0	43.8	68.7	0.6	69.6	0.0	68.5	69.8	68.2
C	21.0	1.0	21.0	0.4	21.3	0.4	21.5	0.2	22.1	0.3									
Structural formulae																			
Si													2.0	0.1	1.5	0.0	2.0	1.6	1.9
Al													0.1	0.1	0.2	0.0	0.2	0.2	0.3
Cr													0.0	0.0	0.1	0.0	0.0	0.1	0.0
Fe	0.1		0.1		0.1		0.1		0.1		0.5	0.2	0.5	0.1	0.8	0.0	0.5	0.7	0.4
Mn	0.1		0.1		0.2		0.1		0.1				0.0	0.0	0.0	0.0	0.0	0.0	0.0
Mg	0.7		0.7		0.7		0.6		0.6				1.4	0.2	1.2	0.0	1.4	1.0	1.6
Ca	0.9		0.9		0.9		0.9		0.8		9.2	9.9	0.0	0.0	0.0	0.0	0.1	0.1	0.0
S													0.0	0.1	0.1	0.0	0.0	0.2	0.1

P											6.5	6.1							
C	2.1		2.1		2.1		2.1		2.2										

*Number of ions on the basis of 9 O for phyllosilicates, 26 for phosphates, 6 for carbonates.

S.D. - standard deviation.